Diploma Thesis

Morphology Investigation and Implementation of Quantitative Friction Force Measurements of Low Friction Coatings

Thomas KLÜNSNER

Department of Physics
Montanuniversität Leoben

Under supervision of
Ao. Univ.-Prof. Dr. Christian TEICHERT

Leoben, February 2008

Eidesstattliche Erklärung

Ich erkläre an Eides statt, dass ich diese Arbeit selbstständig verfasst, andere als die angegebenen Quellen und Hilfsmittel nicht benutzt und mich auch sonst keiner unerlaubten Hilfsmittel bedient habe.

Affidavit

I declare in lieu of oath, that I wrote this thesis and performed the associated research myself, using only literature cited in this volume.

25.2.2008

Thomas Klünsner

Acknowledgements

The present work was performed in cooperation with the project “Low Friction Coatings” supported by the Austrian NANO Initiative given a grant from the Austrian Science Fund FWF.

Especially I want to thank the members of the Scanning Probe Microscopy group at the Department of Physics of the Montanuniversität Leoben for providing me with a pleasant working environment. I really appreciate the time they spent helping me to complete my work. My special thanks go to **Prof. Dr. Christian Teichert** and **Dr. Gregor Hlawacek** who were never tired of discussing my latest findings. Without their helpful guidance and their expert input my work would not have been possible.

My thanks go to **Prof. Dr. Christian Mitterer**, leader of the Thin Film Group at the Institute of Physical Metallurgy of the Montanuniversität Leoben, for giving me the chance to work in the abovementioned project.

Furthermore I want to thank **DI Nazanin Fateh** and **DI Harald Köstenbauer** for providing me with samples of their thin films, which were investigated.

Abstract

A strategy to develop new, lubricant-free engineering concepts is based on low friction- or self-lubricating hard coatings. Information about the surface morphology and the friction coefficients on the nanometer scale is essential for the understanding of the functioning of these materials. The morphology of the low friction coating systems V_2O_5 on Si(100) and MgO(100) as well as TiN-Ag nanocomposites on Si(100) fabricated by unbalanced dc reactive magnetron sputtering was investigated using Atomic Force Microscopy (AFM). Analysing the height-height-correlation function, the evolution of the surface roughness parameters root mean square roughness (RMS), lateral correlation length and the hurst parameter was investigated. Studying samples of V_2O_5 deposited at temperatures from 26°C to 300°C, a transition from amorphous to crystalline growth at 80°C was observed. The RMS roughness increased from 0.7 nm at 26°C to 21 nm at 300°C. On TiN with 45 at.% Ag, a preferential separation of prominent surface features of 250 nm was determined, analysing the radial power spectral density function. Furthermore, a method to quantitatively determine coefficients of friction via Friction Force Microscopy (FFM) has been implemented. Using the cantilever's spring constant determined by thermal tuning the surface contact forces were calculated. The calibration factor Alpha [N/V] that directly links lateral deflection in FFM with friction force was measured using a calibration grating of known geometry. Coefficients of friction were observed to increase with scan speed on a reference sample of Mica(0001). At a scan speed of 2 μm/s, values of the friction coefficient on TiN with 7 at.% Ag and on V_2O_5 were found to be 0.07 and 0.12, respectively.

Keywords: AFM, Surface roughness analysis, FFM, friction coefficient, Low Friction Coatings, V_2O_5, TiN-Ag

Kurzfassung

Eine Strategie zur Entwicklung neuer, schmierstofffreier Engineering-Konzepte basiert auf dem Einsatz von Niedrigreibungs- oder selbstschmierenden Hartstoffschichten. Für das Verständnis der Funktionsweise dieser Schichten ist die Kenntnis der Oberflächenmorphologie und der Reibkoeffizienten auf der Nanometerskala unabdingbar. Morphologieuntersuchungen an den mit Hilfe von "Unbalanced dc reactive magnetron sputtering" hergestellten "Low Friction Coating"-Dünnschichtsystemen V_2O_5 auf Si(100) und MgO(100) sowie die Nanocompositschicht TiN-Ag auf Si(100) wurden mittels Atomic Force Microscopy (AFM) durchgeführt. Mittels der Analyse der Höhen-Höhen-Korrelationsfunktion wurde die Evolution der Rauigkeitsparameter root mean square roughness (RMS), der lateralen Korrelationslänge und des Hurst Parameters bei Abscheidetemperaturen von 26°C bis 300°C untersucht. Für V_2O_5 auf MgO(100) konnte ein Wechsel von amorphem zu kristallinem Wachstum bei 80°C beobachtet werden. Die RMS Rauigkeit stieg von 0.7 nm bei 26°C auf 21 nm bei 300°C. Mit Hilfe der "Radial power spectral density function" wurde auf TiN mit 45 at.% Ag eine mittlere Distanz zwischen den Oberflächenerhebungen von 250 nm bestimmt. Weiters wurde eine Methode zur quantitativen Bestimmung des Reibkoeffizienten mittels Friction Force Microscopy (FFM) implementiert. Die über "thermal tuning" bestimmte Federkonstante des Biegebalkens diente zur Berechnung der Kontaktkräfte. Ein Kalibrierungsfaktor Alpha [N/V], der das laterale Messsignal in FFM mit den auftretenden Reibkräften in Verbindung bringt, wurde unter Verwendung eines Kalibrationsgitters mit bekannter Geometrie ermittelt. Auf der Referenzprobe Glimmer(0001) stieg der gemessene Reibkoeffizient mit zunehmender Spitzengeschwindigkeit an. Bei einer Geschwindigkeit der AFM-Spitze von 2 μm/s betrug der Wert des Reibungskoeffizienten 0.07 auf TiN mit 7 at.% Ag und 0.12 auf V_2O_5.

Schlagwörter: AFM, Rauigkeitsanalyse, FFM, Reibkoeffizient, Low Friction Coatings, V_2O_5, TiN-Ag

Motivation

A major energy dissipation mechanism in today's engineering components is found to happen between its moving parts: friction. Engineers have thought of different possible friction reduction strategies to enhance the performance of their machines and tools. One of the numerous strategies engineers and material scientists have developed to reduce the coefficient of friction and wear is the use of solid lubricants in form of thin films. The present work is an attempt to understand the microstructure evolution of these Low Friction Coatings by means of *Atomic Force Microscopy* (AFM) measurements that reveal surface features down to the nanometer scale. Furthermore, a quantitative method to determine friction forces in the nano-Newton regime using *Friction Force Microscopy* (FFM) has been implemented. The method yields information on the coefficients of friction of the Low Friction Coatings. The investigated thin film systems were TiN-Ag nanocomposites films and V_2O_5, grown on MgO(100) and Si(100) substrates. In the case of V_2O_5, the formation of so-called Magnéli phases that produce a lubricating liquid film on their surface when used at high homologous temperatures leads to a decrease in the friction coefficient. In addition, the orthorombic α-V_2O_5 phase - present at room temperature - exhibits easy shear planes with reduced binding strength. TiN is a common hard coating that increases surface durability and wear properties of, e.g., cutting tools.

The author hopes that the implemented method will be of use for future engineering of hard coatings and other thin films.

Table of content

1 Theoretical background

1.1 Principle of AFM and FFM

Atomic Force Microscopy (AFM) is a member of the family of scanning probe methods. The fathers of Scanning Tunneling Microscopy (STM) the first technique of this family that was to be developed in 1981 at IBM Zürich are Gerd K. Binnig and Heinrich Rohrer [1]. They shared the 1986 Nobel Prize in physics with German scientist Ernst Ruska, designer of the first Electron Microscope (SEM). Using the STM it was possible for the first time in history to reach atomic resolution – to make atoms visible. One of the great difficulties Binning and Rohrer had to overcome was the fact that in scanning probe techniques the motion of a vulnerable tip of a needle needs to be controlled very accurately. The height at which for example an STM tip travels over the sample surface is in the regime of only a few atomic diameters.

The disadvantage of the STM method is the mandatory electric conductive nature of objects that under investigation. This problem was overcome by the invention of AFM by G. Binnig, C.F. Quate and Ch. Gerber [2] in 1986 in which electric conductivity of the sample is not a prerequisite. AFM techniques in general require a thin, elastic beam that holds a tip of about ten nanometers in radius that is moved over a sample by a piezoelectric scanner. Interactions between tip and sample surface bend the cantilever as it is approaches the surface. The most popular method to determine the current position of the lever was developed by Meyer and Amer and uses the signal recorded by a four quadrant photodiode that registers the offset of a laser beam that is reflected off the cantilever's upper side [3]. The tip's movement is thereby measured as a voltage change applied to the scanner that can be converted to the tip's position.

There are many different modes in which an AFM can be used to acquire a signal from a sample. In general one can think of Non-Contact Mode (NCM), Tapping Mode (TM) and Contact Mode (CM). Since they were used in the present work, TM-AFM and a type of CM-AFM measurements the so-called *Lateral Force Microscopy* (LFM) or also *Friction Force Microscopy* (FFM) are to be explained briefly. In the future the method will be referred to as FFM rather than LFM even though both terms are common in the literature.

1.1.1 Contact Mode AFM

In this type of AFM technique the tip is in physical contact with the sample surface. When the tip encounters a bump or asperity when being scanned across the sample surface the cantilever will bend, the photodiode will yield a signal and the scanner will respond according to the gain settings of the scanner's control loop imposed by the operator (see Fig. 1). If the gain is set to zero no response will occur and the cantilever will bend according to its spring constant. This mode is called "constant height" or "varying force" mode. It's used for very flat surfaces such as atomic structures. The second mode of operation is called "constant force mode" in which the gains need to be imposed to fit the individual morphology or roughness of the sample. The AFM will try to keep the force applied to the sample constant or in other words the bending of the cantilever is constant. Gains that are set too low will result in poor image quality because the tip cannot follow the surface morphology any more. Gains set to high will lead to hypersensitivity due to random noise.

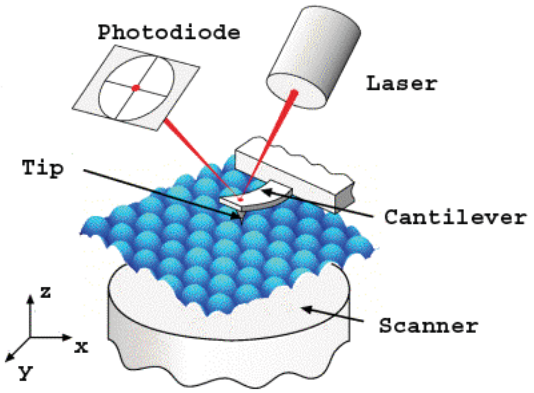

Fig. 1: Scheme of an Atomic Force Microscope, after [4]

1.1.2 Friction Force Microscopy

In AFM techniques the cantilever is moved over a sample's surface in a certain pattern of motion consisting of two parts - the so-called fast- and slow scan directions. In the fast scan direction the cantilever performs a back-and-forth movement within the boundaries of a designated scan area to collect two scans in "trace" and retrace" from the same line. After this step the cantilever changes its position in the direction of the slow scan axis to collect two scans of the next line. In this manner information about the designated scan area is acquired. In FFM the fast scan direction is not, as usual, parallel to the cantilever's long axis but perpendicular to it. As a result the cantilever is not only bent but also twisted during scanning. The course of the laser beam will not only be diverted in vertical but also in horizontal direction. The lateral deflection is in part due to friction forces and also to topography. When encountering a high

friction area on a sample the lateral deflection detected by the photodiode will be greater in magnitude than on areas that are lower in friction. The changes in lateral deflection caused by friction are of opposite prefix in trace and retrace whereas topography induced signal changes are of the same prefix (see Fig. 2). Subtracting the trace from the retrace signal only the friction induced deflection change remains.

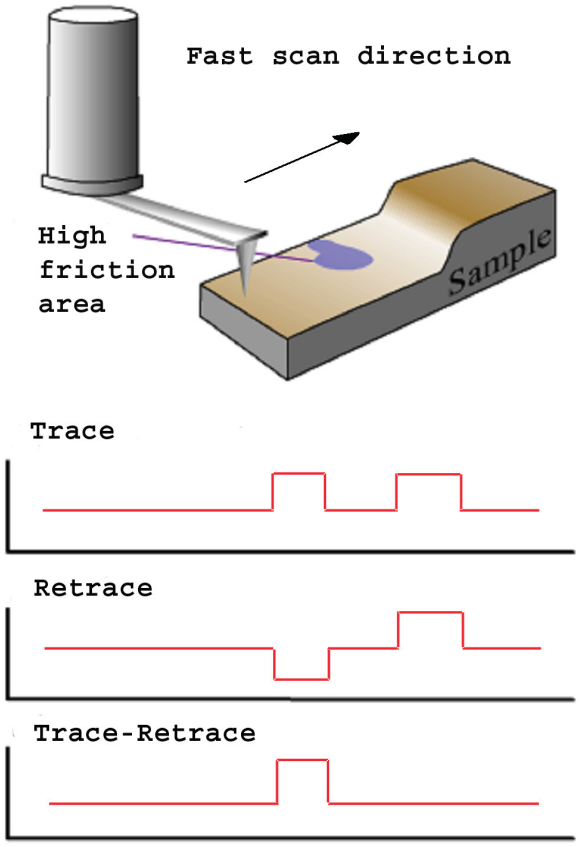

Fig. 2: Lateral deflection in trace and retrace in FFM, after [5]

1.1.3 Tapping Mode AFM

Tapping Mode, also called intermittent contact mode, is a dynamic AFM mode in which the cantilever that holds the tip is excited to oscillate near its resonance frequency. The moving cantilever approaches the sample surface until interactions between the tip and the sample start to modify the frequency at which the lever oscillates. According to the gain settings the AFM will try to keep the amplitude of the cantilever thus the distance from the surface constant. From the change in position of the piezo scanner, information about the sample topography is derived. The advantage over contact modes is that in general less force is applied to the surface so it is in general less influenced by the measurement. In the present work TM-AFM measurements were used to characterize film morphology and for calculation of surface roughness parameters.

1.2 Determination of cantilever spring constants by thermal tuning

During scanning of a sample surface the cantilever's bending is registered by the photodiode. To convert this displacement signal to a force value it needs to be multiplied by the spring constant *k* of the cantilever. The spring constant given by the manufacturer was checked by a method suggested by Sader *et al*. [6] in which unloaded thermal resonance frequency of a rectangular cantilever in air ω_f and its plan view dimensions are directly related to its spring constant by Eq. (1)

$$k = 0.1906 \quad \rho_f b^2 l Q_f \Gamma_i(\omega_f) \omega_f^2 \qquad (1)$$

where b is the cantilever's width, l its length, ρ_f the density of the fluid surrounding the cantilever, Q_f the quality factor in air, Γ is the hydrodynamic function of the cantilever that depends on ω_f . For an analytical expression for Γ the reader is referred to Eq. (20) of Ref. [7]. The cantilevers' resonance frequencies in thermal equilibrium were determined by fitting the peak in their thermal spectrum that is collected from the unloaded cantilever excited to oscillate by Brownian motion. To calculate the spring constants an online applet was used [8].

1.3 Determination of contact forces via force distance curves

To calculate the friction coefficient μ one needs to know the value of force applied to a surface. To calculate contact force values the so-called force distance curve (see Fig. 3) is collected.

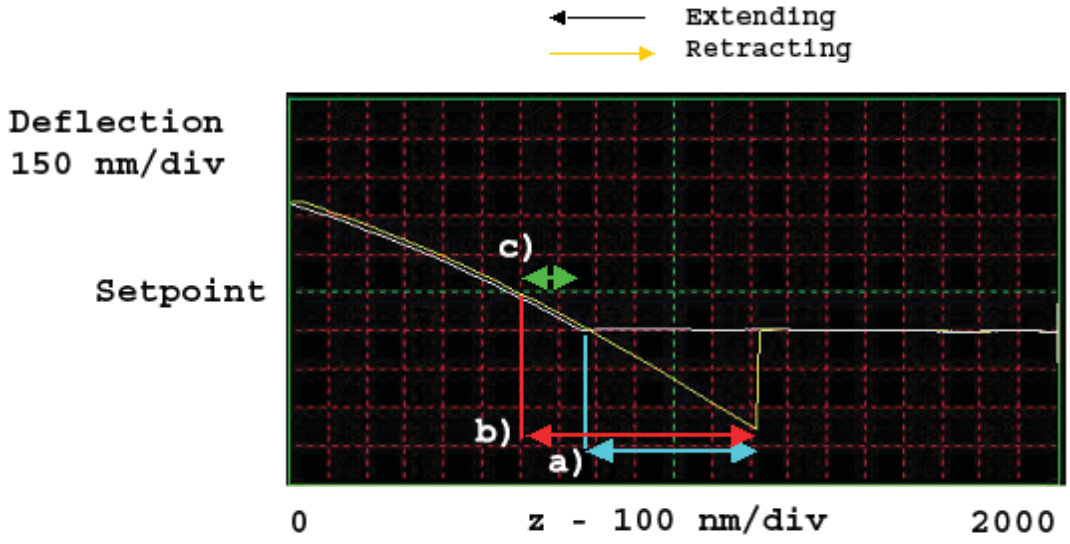

Fig. 3: Force distance curve

As the tip approaches the surface in z-direction the cantilever remains unbent until capillary forces exerted by an adsorbed water film usually present on the sample surface in ambient air start to act between the tip and the sample surface causing the tip to "snap in". The direct contact with the sample surface after penetrating the water layer will cause the cantilever to bend which will lead to an increase in the laser's deflection detected by the photodiode. Retracting the lever will decrease the deflection even down to a value that is lower than the one prior to first contact with the surface. Again under ambient conditions the main source of this adhesive force A is the formation of a capillary bridge between the tip and the sample. When this bridge is destroyed the cantilever snaps back into an unbent state.

Interested in a certain value of force one needs to multiply the relevant Δz-displacement in the force-distance curve with the cantilever's spring constant. For the relevant Δz value for A one measures from the lowest deflection value of the retraction curve to the intersection of the same with the level of deflection of the unloaded cantilever (see a) in Fig. 3). The total load L which corresponds to A plus the load applied by the piezo scanner can be calculated using Δz from the lowest value of deflection to the intersection of the retraction curve with the setpoint

level of deflection (see b) in Fig. 3). The value of the load applied by the piezo scanner is represented by Δz from the intersection of the retraction curve with the setpoint deflection level to the point of first contact of the tip with the surface (see c) in Fig. 3).

1.4 Varenberg calibration method

The following method to obtain a calibration factor that links the voltage values measured in FFM measurements with the actual friction force values was suggested by M. Varenberg [9]. It was implemented for integrated probes to be able to look at the coefficients of friction on Low Friction Coatings.

Fig. 4 shows all the forces and momentums acting on the cantilever scanning the tip across a sloped surface.

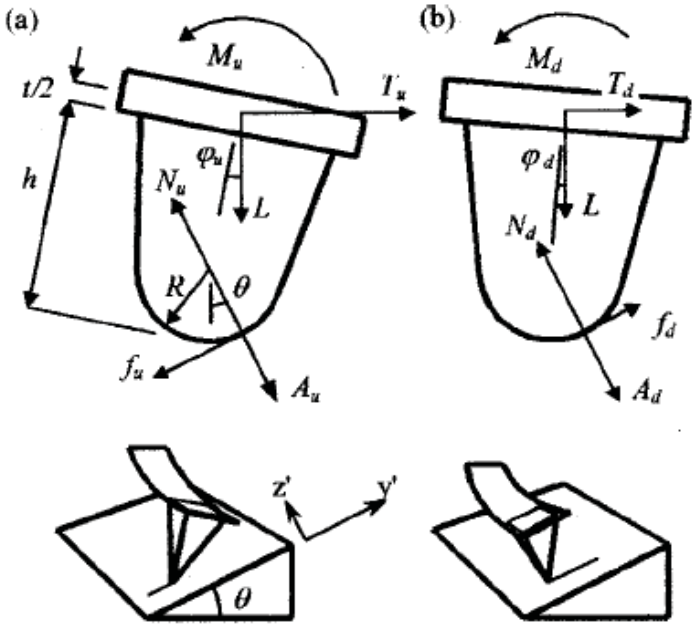

Fig. 4: Free body diagrams of the cantilever while scanning (a) up or (b) down a sloped surface [9] see text

The forces applied to the surface are the contact load N, the adhesion force A, and the friction force f. They are balanced by the load L, the transversal force T, and the torsion moment M. The forces depend on the direction of motion – balancing the forces for the uphill direction one can think of the following equation for the y'-direction:

$$T_u \cos \Theta - L \sin \Theta + f_u = 0 \qquad (2)$$

and for the z' direction

$$-T_u \sin\Theta - L\cos\Theta + N_u - A_u = 0 \tag{3}$$

Doing the same for the downhill motion we get:

$$T_d \cos\Theta - L\sin\Theta + f_u = 0 \tag{4}$$

and

$$-T_d \cos\Theta - L\cos\Theta + N_d - A_d = 0 \tag{5}$$

Assuming $f = \mu N$ where μ is a constant, and $A_u = A_d = A$ in the range between N_u and N_d , we obtain from Eqs. (2) and (3) for the uphill motion:

$$T_u = \frac{L\sin\Theta + \mu(L\cos\Theta + A)}{\cos\Theta - \mu\sin\Theta} \tag{6}$$

and from Eqs. (4) and (5) for the downhill motion

$$T_d = \frac{L\sin\Theta - \mu(L\cos\Theta + A)}{\cos\Theta + \mu\sin\Theta} \tag{7}$$

Balancing the moments in play, assuming small cantilever torsion angles $\varphi(\sin\varphi = \varphi, \cos\varphi = 1)$, give us for the uphill motion

$$\begin{aligned} &M_u + L[R\sin\Theta - (h - R + t/2)\varphi_u] \\ &- T_u(R\cos\Theta + h - R + t/2) = 0 \end{aligned} \tag{8}$$

and

$$\begin{aligned} &M_d + L[R\sin\Theta - (h - R + t/2)\varphi_d] \\ &- T_d(R\cos\Theta + h - R + t/2) = 0 \end{aligned} \tag{9}$$

for the downhill motion.

In Eqs. (8) and (9) R is the tip radius of curvature, h the tip height, t the cantilever thickness. It is assumed that the force T acts through the mid section of the cantilever. The torsion moment M and the torsion angle φ can be linked by the relation

$$\varphi = \frac{Ml}{GJ} \tag{10}$$

where l is the cantilever length, G the shear modulus, and J the torsion constant of the cross section of the cantilever (not to be confused with the polar moment of inertia). Combining Eqs. (8) and (10) gives us

$$M_u C + LR\sin\Theta - T_u(R\cos\Theta + h - R + t/2) = 0 \qquad (11)$$

where

$$C = \frac{GJ/l - L(h - R + t/2)}{GJ/l}.$$

Considering typical values of G = 64 GPa (for silicon), cantilever width, w = 30 μm, t = 1 μm, l = 100 μm, we have GJ/l = $0.6\text{x}10^{-8}$ Nm ($J \approx 0.3\ wt^3$) for the rectangular cross section of w/t >10) [10]. For h = 20 μm, R = 10 nm and L = 5 μN, we have L(h-R+t/2) = 10^{-10} Nm. Therefore $C \approx 1$ and Eq. (11) for the uphill motion becomes

$$M_u + LR\sin\Theta - T_u(R\cos\Theta + h - R + t/2) = 0 \qquad (12)$$

Similarly, combining Eq. (9) and Eq. (10) gives for the downhill motion

$$M_d + LR\sin\Theta - T_d(R\cos\Theta + h - R + t/2) = 0 \qquad (13)$$

What Varenberg's method [9] ultimately wants to achieve is to connect the moment M, which is measured by the AFM via the cantilever torsion angle φ which yields a voltage signal from the photodiode, with the actual friction force on a flat surface. The unconverted value in volts will be called M_o, where the index "o" indicates the unit volt. M_o is related to M by $\beta M_o = M$. The calibration constant β [Nm/V] is a product of all the factors of the system. Remembering that on flat surfaces Θ = 0 and combining Eqs. (2) and (12) we have

$$f^{flat} = T^{flat} = \frac{M^{flat}}{h + t/2} = \alpha M_0^{flat} \qquad (14)$$

where the calibration constant α [N/V] is

$$\alpha = \frac{\beta}{h + t/2} \qquad (15)$$

The desired constant α converts a moment voltage output M_o to a friction force f^{flat}.

Varenberg [9] addresses the calibration of integrated and colloidal probes, here we will only consider integrated ones:

For integrated probes it is feasible to assume that the tip height h is a few orders of magnitude larger than the tip radius of curvature R (h>>R). This assumption can be used to simplify Eqs. (12) and (13) to

$$M_u = T_u(h + t/2) \qquad (16)$$

and

$$M_d = T_d(h + t/2) \tag{17}$$

for the uphill and downhill motions, respectively.

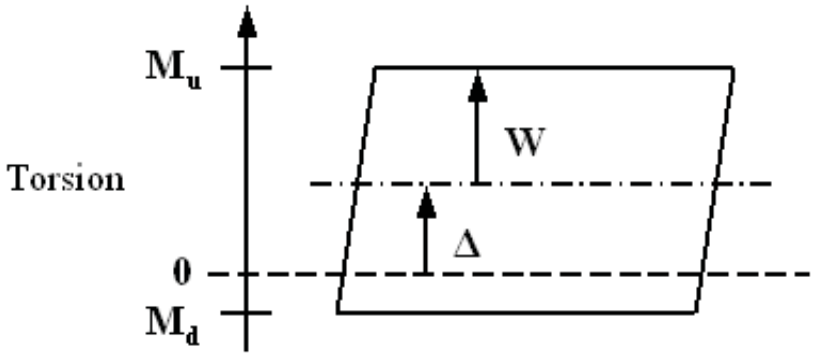

Fig. 5: Schematic torsion loop: torsion moments for downhill, M_d, and uphill, M_u, scans, after [9]

The torsion loop, which represents the trace and retrace signal obtained on a sloped surface, is illustrated in Fig. 5, where

$$W = \frac{M_u - M_d}{2} \tag{18}$$

represents the half-width of the loop, and

$$\Delta = \frac{M_u + M_d}{2} \tag{19}$$

represents the offset of the loop. The measured voltage output M_0 where $\beta M_o = M$ defines $\beta W_o = W$ and $\beta \Delta_o = \Delta$. The problem now is that signal drift, crosstalk between deflection and torsion signals, and even small misalignment of the laser or cantilever with respect to the photodiode, make it impossible to determine the exact zero-level of the torsion signal (see Fig. 5) and the actual torsion loop offset Δ_o. Luckily, the torsion loop half-width W_o is insensitive to this problem since it is a relative value. To overcome the problem of the uncertainty of the torsion signal's zero point, Varenberg [9] suggests the following: By using a calibration grating of known geometry with sloped (Si (111)) and flat (Si (100)) facets (see Fig. 6)

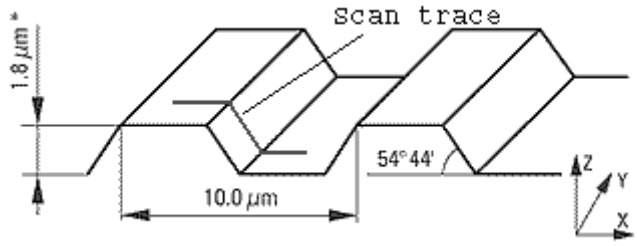

Fig. 6: Schematic sketch of TGF11 silicon calibration grating [11]

we can correct the inaccurate measured torsion loop offset Δ_o* by subtracting from it the torsion loop offset measured on the flat surface, Δ_o^{flat}, since on the flat part of the grating we can be sure that the cantilever's twist is only caused by the friction force and not by topography. This gives us the accurate torsion loop offset

$\Delta_o = \Delta_o$*- Δ_o^{flat}.

Now, substituting Eqs. (6), (7), (15), (16) and (17) in Eq. (18) and remembering that $W = \beta W_o$, we have

$$\frac{\mu(L + A\cos\Theta)}{\cos^2\Theta - \mu^2\sin^2\Theta} = \frac{W}{h + t/2} = \alpha W_0 \qquad (20)$$

Analogical, from Eq. (19) with the correction $\Delta = \beta(\Delta_o$*- $\Delta_o^{flat})$, we have

$$\begin{aligned} &\frac{\mu^2 \sin\Theta(L\cos\Theta + A) + L\sin\Theta\cos\Theta}{\cos^2\Theta - \mu^2\sin^2\Theta} \\ &= \frac{\Delta}{h + t/2} \\ &= \alpha(\Delta_o^* - \Delta_o^{flat}) \end{aligned} \qquad (21)$$

Dividing Eq. (22) by Eq. (20) gives us a quadratic equation for the unknown μ in the form

$$\begin{aligned} &\sin\Theta(L\cos\Theta + A)\mu^2 \\ &- \frac{\Delta_0^* - \Delta_0^{flat}}{W_0}(L + A\cos\Theta)\mu \\ &+ L\sin\Theta\cos\Theta = 0 \end{aligned} \qquad (22)$$

Equation (22) contains the known slope Θ (in radians), load L and adhesion A (in newtons) and the measured actual torsion loop offset (Δ_o*- Δ_o^{flat}) and the torsion loop half-width W_o (in volts). Being a quadratic equation, Eq. (22) provides two possible solutions of the friction coefficient μ for the slope of any given load L and adhesion A. How can we now decide which of the two is correct? The real solution must be smaller than $1/\tan\Theta$, since otherwise the calibration factor α is a negative value when substituted in Eq. (20) or (22). If both of the values of μ satisfy the condition $\mu < 1/\tan\Theta$, we use the following method to find the appropriate α (see Fig. 7). Each of the two possible values of μ, when substituted in e.g. Eq. (20) yields a corresponding calibration factor α_i. Since the calibration factor must be the same for the slope and

the flat part of the grating, we can use the two α_i values in Eq. (20) with: $\Theta = 0$ and $W_o = W_o^{flat}$ to find two values of the friction coefficient μ_i^{flat} for each α_i:

$$\mu^{flat} = \frac{\alpha W_o^{flat}}{L + A} \tag{23}$$

In general the μ_i on different crystallographic planes may differ but their absolute difference should not be too large. To find the α_i with true physical meaning we now subtract μ from μ^{flat}. The calibration factor α that gives the closest values of μ_i and μ_i^{flat} is the link between lateral deflection and friction force that was sought-after.

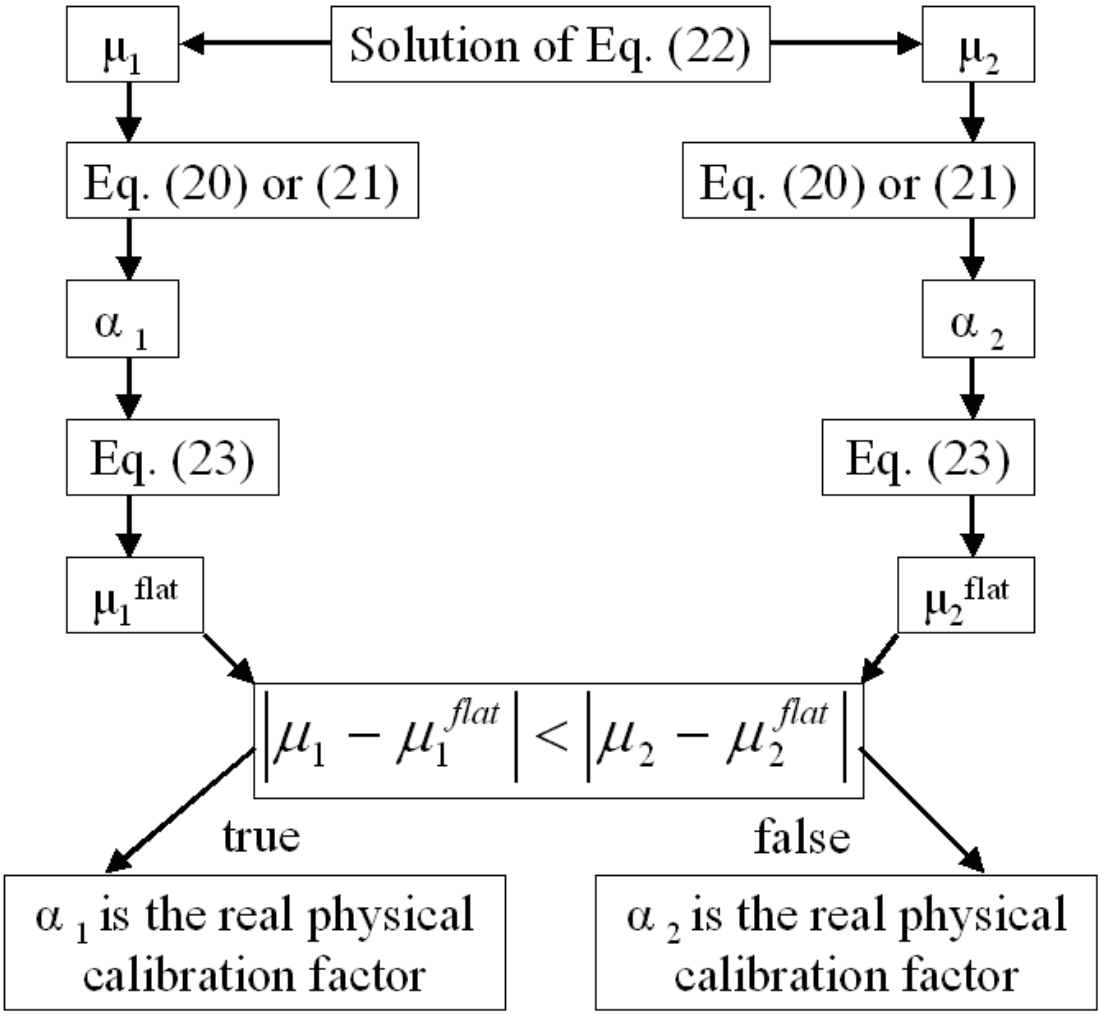

Fig. 7: Step by step description of the solution for calibration factor α , after [9]

1.5 Recording procedure of friction force images

In order to gather quantitative information about friction forces on a surface one needs to record an FFM image in constant force mode. To determine the load L and adhesion A, a force distance curve needs to be

recorded as described above before every measurement. The value of L was also checked after every other measurement and was found to be unchanged. After retraction of the tip from the sample surface this step has to be repeated since the setpoint of the AFM is subject to drift. Offsets of all friction channels must be set to zero since deflection values need to remain unaltered.

To find the calibration factor α [N/V] of an individual probe a number of line scans in trace and retrace of the flat and the inclined part of the calibration grating TGF11 have to be recorded (see a) in Fig. 8). The values of Δ_o* and W_o of the inclined part and Δ_o^{flat} and W_o^{flat} of the flat part of the grating are averaged by calculating the mean values of many line scans. Part b) in Fig. 8 shows the desired appearance of the levels of deflection on the inclined part of the grating where the levels of deflection are lower than on the flat part of the grating. On the other side of the trench this characteristic is reversed. For tip calibration picture resolution was lowered to 128 x 128 pixels in contrast to the 512 x 512 pixels recorded on sample surfaces. Changes in scan speed performed during calibration from 5 μm/s to 10 μm/s appeared to have no significant influence on calibration results.

When investigating a sample one needs to be aware that the smoother a sample's surface the better the determination of friction forces works. This is due to the fact that every time the cantilever encounters a sudden change in topography a spike in deflection occurs that needs to be filtered before calculating the friction force. These spikes are due to the fact that the height change occurs to suddenly for the scanner to react and to adjust the tip's position in the z-direction. Fig. 9a shows a V_2O_5 facet, Fig. 9b the corresponding "trace minus retrace" image (see 1.7). On the borders of the facet high deflection spikes can be observed. The filter option "mark by threshold" in the Gwyddion software [12] was used to filter these variations in deflection. The fluctuations in the plateaus of deflection between the topography induced spikes were found not to reoccur on the same spots when recording several images on the same location on the sample and therefore are thought to be caused by random noise.

Scan speeds on samples were varied from 0.4 μm/s at a scan size of 100 x 100 nm to 2 μm/s at a scan size of 1x1 μm on all samples to get an idea about possible tip-speed dependence on friction. On mica the tip-speed was increased up to 4 μm/s at a scan size of 1x1 μm.

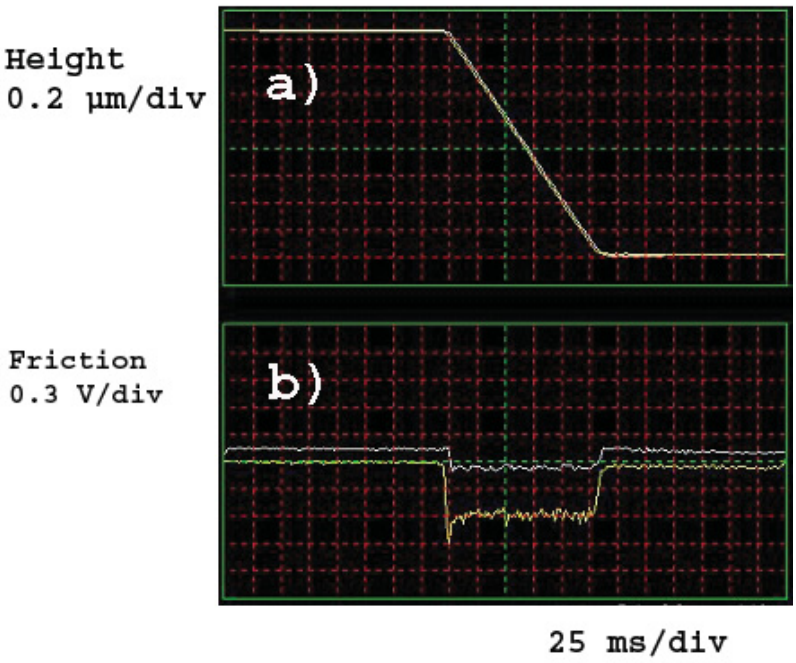

Fig. 8: a) Suggestion for the selection of scan area on TGF11 for calibration process b) desired appearance of trace and retrace

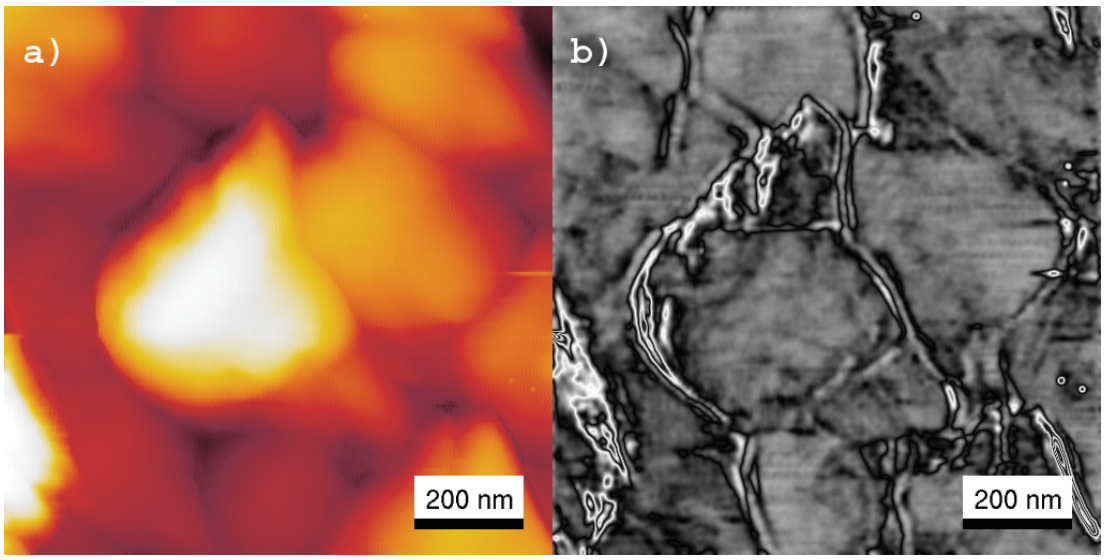

Fig. 9: a) Topography of V_2O_5 on Si(100) b) corresponding trace minus retrace image of lateral deflection; z-scale: 75 nm in a), 2 V in b)

1.6 Quantitative surface roughness analysis

Rough surfaces can be divided in three categories. **Self-similar fractal surface** structures look the same no matter how much we magnify its image. **Self-affine fractal surfaces** have z-variations that are much smaller than their lateral fluctuations. **Self-affine fractal surfaces with a cut-off** show self-affine behavior on short length scale but are smooth on a long length scale [13,14].

Vertical roughness is often quantified as root mean square roughness σ (RMS) which is the standard deviation of surface heights from the mean height value <z> of a certain area.

$$\sigma = \sqrt{\frac{1}{L}\int_0^L \left(z - < z >\right)^2 dx} \tag{24}$$

To improve statistical relevance the median of three RMS values of 5 x 5 μm scans was calculated.

The **lateral correlation length** ξ indicates the maximum lateral separation for that the heights of two surface points are correlated.

Rule of thumb:

ξ is smaller than the average feature size. ξ corresponds to the minimum lateral feature size.

The **Hurst parameter h** also called roughness parameter α gives information on how jagged a surface is. A value of h = 1 indicate sinusoidal-like surface ondulations, at low values e.g. h = 0.5 surface structures are pointy.

Correlation functions describe the relation random data points have with neighboring ones. One that can be used to describe isotropic surfaces is the so-called **height-height-correlation function C(x) (HHCF):**

$$C(x) = < [z(x_o + x) - < z >][z(x_o) - < z >] > \tag{25}$$

Where <...> is the median of all x_0 of a line scan.

For self-affine surfaces with a cut-off C(x) can be fitted with

$$C(x) = \sigma^2 \exp[-(|x| / \xi)^{2h}] \tag{26}$$

The roughness parameters σ, ξ and h described above can be acquired fitting this function.

$$C(0) = \sigma^2 \tag{27}$$

$$C(\xi) = \frac{\sigma^2}{e} \tag{28}$$

Another possibility to acquire h is to calculate the gradient at x << ξ of the so-called **height difference function H(x):**

$$H(x) = < [z(x_o + x) - z(x_o)]^2 > \tag{29}$$

$$H(x) \approx x^{2h} \quad for\ x << \xi \tag{30}$$

$$H(x) \approx 2\sigma^2 \quad for\, x >> \xi \tag{31}$$

In the case of a periodic arrangement of features on a surface, the **power spectral density function S(k)** which is defined as

$$S(k) = \left| F\{C(x)\} \right| ,$$

$$S(k) = \left| F\left\{ x_{ij} \right\} \right|^2 , \tag{32}$$

where k is a wave vector, yields information on the average lateral separation of the surface features. In S(k) of a surface with complete long-range order, pronounced peaks appear of which the first yields the preferential separation of the surface features in real space. S(k) is also called the **power spectral density (PSD)** or **power spectrum** of the surface roughness. In the case of non-perfect ordering the peaks broaden and less higher order peaks are visible [13].

1.7 Data analysis using Gwyddion software

The free software Gwyddion [12] version 2.7 was used to analyze the recorded scans. It enables the user to select regions the image e.g. by threshold or slope angle and to calculate the median value of the selected data points, RMS roughness and many other parameters. This function is of great utility making deflection data statistically relevant by averaging over many scan lines.

In this work, the author took advantage of the ability of Gwyddion to subtract images from another by subtracting a data point in the trace image, collected through FFM scans, from the corresponding point in the retrace image. These pictures are referred to as “trace minus retrace” images. In this manner morphology induced artifacts in FFM images are reduced.

For the determination of a median grain diameter of the TiN films the watershed algorithm was used which inverts the surface’s topography in z-direction and lets it rain virtually onto the inverted surface. Surface depressions represent local minima in the inverted landscape where the virtual raindrops rest to await more drops to form pools. In this manner a mask is generated which then can be used to acquire information about the surface features. More information can be found in the online documentation of Gwyddion [12].

2 Experimental setup

2.1 AFM Instrumentation

All measurements described below were carried out with a Digital Instruments (DI) Nanoscope Multimode IIIa Scanning Microscope with an AS-130 ("J") piezoelectric scanner (see Fig. 10). Maximum scan size of this device is 125 x 125 µm, maximum travel distance of the z-piezo is 5 µm. The DI software package version 5.30r3sr3 was used.

Fig. 10: Digital Instruments (DI) Nanoscope Multimode IIIa Scanning Microscope

Pointprobe®plus PPP-NCHR tips of silicon (see Fig. 11) by the company Nanosensors™ with a cone angle of 20 degrees were used for TM measurements. For all FFM measurements PPP-LFMR tips of silicon were used that were 225 ±10 µm in length and 48 ±10 µm in width. The samples were glued to small steel plates for handling. Relative humidity in the lab varied from 27% at a temperature of 21°C to 48% at 23°C.

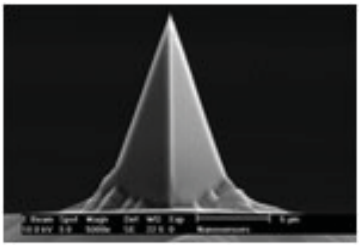

Fig. 11: Tapping Mode AFM tip Pointprobe®plus NCHR [15]

The resolution of all the TM images recorded was 512 x 512 pixels. FFM images were also recorded at 512 x 512 pixels resolution, 128 x 128 pixels for calibration scans on TGF11. In Topography images a third order plane fit was applied to the images to compensate for scanner bow. Individual scan lines were flattened by subtracting a first order polynomial. In friction channels all offsets were set to zero.

Cantilever spring constants were determined with an AFM made by Asylum Research called MFP in combination with the Igor Pro MFP 3D software package (see Fig. 12). A commercially available silicon calibration grating named TGF11 [16] (see Fig. 6) with exact pitch value of 10 μm and inclined slopes of 54°44', formed by the crystallographic (100) and (111) planes, was used for lateral force calibration.

The given values of roughness parameters where averaged over the results of at least three different scans with 5 x 5 μm size.

Fig. 12: Asylum Research AFM "MFP"

2.2 Sample preparation

2.2.1 V_2O_5 thin films

The V_2O_5 films were fabricated by DI Nazanin Fateh using unbalanced DC magnetron sputtering and pulsed unbalanced magnetron sputtering investigated them during her Ph.D. thesis by X-ray diffraction (XRD), Raman spectroscopy, scanning electron microscopy (SEM), selected area electron diffraction (SAED) and transmission electron microscopy (TEM). Cross sectional TEM samples were prepared by focused ion beam (FIB). [17,18,19].

Thin films of an average film thickness of 1.2 μm were grown on MgO (100) substrates via unbalanced DC magnetron sputtering which were ultrasonically pre-cleaned in acetone and ethanol. Deposition chamber pressure was 8×10^{-4} Pa when substrates were thermally cleaned at 750°C for 10 min. Sputtering was done in an Ar/O_2 atmosphere. The total gas pressure in both sputtering modes was 0.28 Pa. Three metallic

vanadium targets (Ø 50.8 mm) with a purity of 99.8% were used. The O_2 partial pressure was 21% of total pressure for all deposited V_2O_5 films. Substrates were rotated at about 10 rpm during deposition to ensure uniform film growth. All films were deposited at floating potential for 60 minutes. Samples were produced at various substrate temperatures of T_s = 26, 80, 100, 150, 230 and 300 °C. Samples were heated from their back side. Sample heating was regulated using an Ogden Microprocessor; sample temperature was measured by a type K, Ni–Cr/Ni thermocouple placed at the steel substrate holder.

For friction measurements thin films of V_2O_5 were deposited on Si(100) substrates at 300°C in the same way described for samples on MgO(100) with the additional making of samples using pulsed unbalanced magnetron sputtering [19]. To deposit films of a thickness of 1.2 μm the higher growth rates in dc sputtering compared to the pulsed dc process were compensated for by depositing for 60 min and 90 min, respectively. For the films prepared by pulsed dc magnetron sputtering, three bipolar pulsed dc power supplies were used for plasma generation. Target pulsing frequency was kept constant at 100 kHz with a 16% duty cycle.

2.2.2 TiN and TiN/Ag nanocomposite films

The investigated films were fabricated and investigated by DI Harald Köstenbauer who undertook profound investigations of the samples. The films were characterized by SEM, TEM and scanning transmission electron microscopy (STEM) of cross-sections, energy-dispersive X-ray (EDX) analysis, XRD and biaxial stress-temperature measurements (BSTM) [20].

TiN/Ag nanocomposite films of a total thickness of about 3 μm were deposited onto 300 μm thick Si(100) substrates which were ultrasonically pre-cleaned in acetone and ethanol. Prior to deposition, the substrates were plasma etched. The deposition was performed by unbalanced dc reactive magnetron sputtering from one Ag and two Ti targets (∅ 50.8 mm) in an Ar/N_2 atmosphere. Substrates were rotated with approximately 10 rounds per minute (rpm) during deposition to ensure uniform film growth. Sputtering power at the Ag target was varied to produce samples with different Ag content. Films with a silver content of 7 at.% Ag and 45 at.% Ag were examined in the present work. Substrate temperature was 150°C, total pressure 0.25 Pa. All films were deposited at floating potential. To improve adhesion, a 50 nm thick TiN interlayer was deposited at a temperature of 450°C directly after substrate etching. After this step substrates were cooled to 150°C to deposit the nanocomposite without excessive Ag diffusion.

The reference sample of pure TiN was deposited using the method described above without the use of the Ag target, without substrate rotation and with a bias voltage of –50V. The deposition temperature was 550°C.

2.2.3 Gold (111) surface

Professor Adolf Winkler of the Department of Solid State Physics of the Institute of Technology Graz provided single-crystalline Au with a (111) surface orientation.

2.2.4 Atomically flat mica

A mica crystal with (0001) orientation was freshly cleaved shortly prior to measurements and attached to a small steel plate using double-faced scotch tape.

3 Results

3.1 Morphology investigation of thin films at various deposition temperatures

3.1.1 V_2O_5 thin films

The investigated coatings were deposited at different temperatures from 26 to 300°C, which had a certain impact on film morphology. Films prepared at room temperature were found to be amorphous [17]. Corresponding TM-AFM images show a rather smooth morphology (see Fig. 13). Note the about 5 nm high surface contaminations. The calculated RMS value σ was 0.7 ± 0.1 nm.

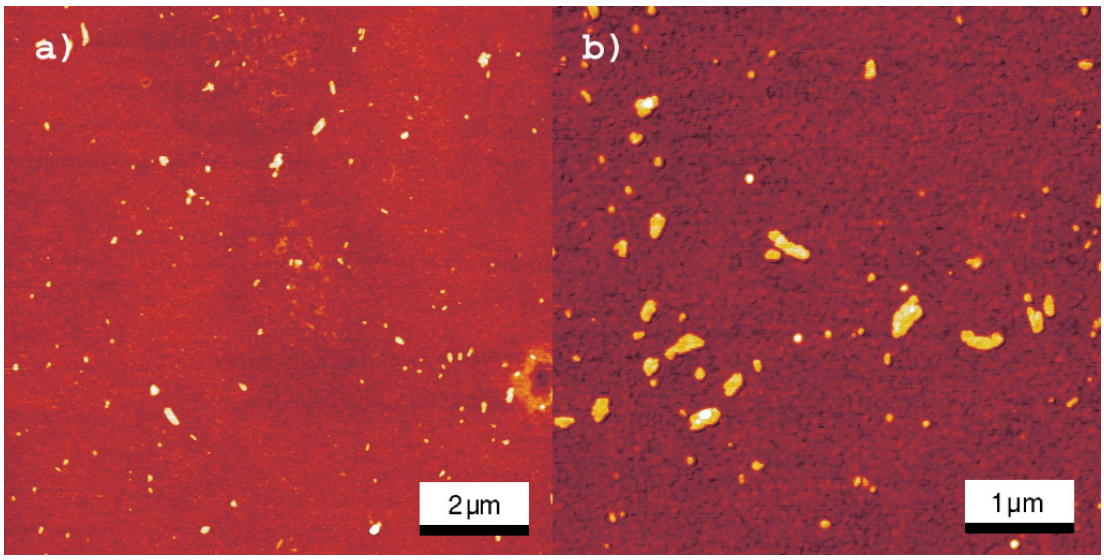

Fig. 13: Topography of V_2O_5 on MgO(100); deposition temperature 26°C, z-scale 10 nm in a) and b)

The onset of crystalline growth occurs at about 80°C when pits of about 50 nm in depth can be found on the sample deposited at this temperature (see Fig. 14a and Fig. 15). The pits harbor little surface features of approximately 50 to 100 nm in diameter (see Fig. 14b and Fig. 16) that are thought to be clusters of crystalline V_2O_5 grains. This assumption is supported by XRD measurements [17]. The RMS value σ of the surface with the pits was 10.0 ± 0.6 nm and 2.5 ± 0.1 nm when filtering the pits by height threshold for calculation of σ. Above 80°C the film grows in a polycrystalline manner with an increase in crystallinity with rising deposition temperature [17]. The transition from amorphous to crystalline growth is attributed to enhanced ad-atom diffusion on the surface with increasing deposition temperature [21].

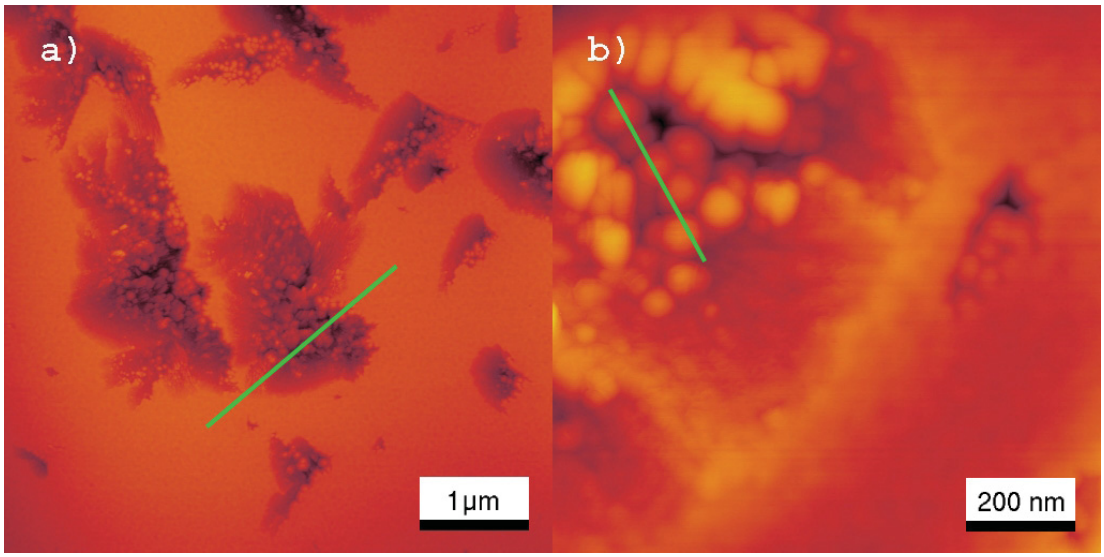

Fig. 14: Topography of V_2O_5 on MgO(100); deposition temperature 80°C, z-scale: a) 150 nm, b) 75 nm

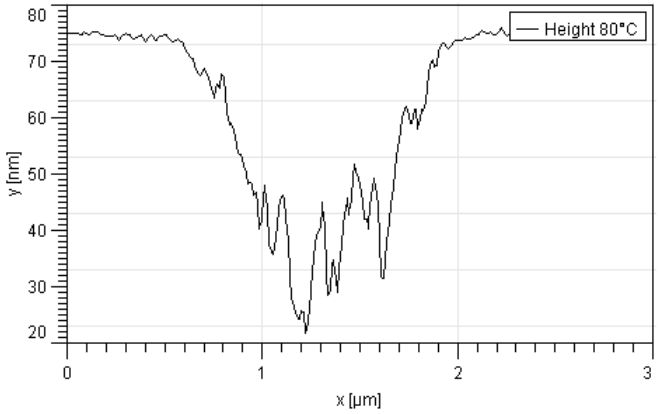

Fig. 15: Cross section of pit as indicated in Fig. 14a)

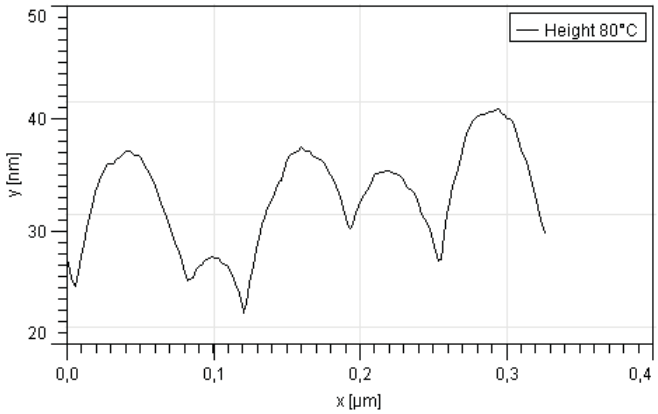

Fig. 16: Cross section of pit as indicated in Fig. 14b)

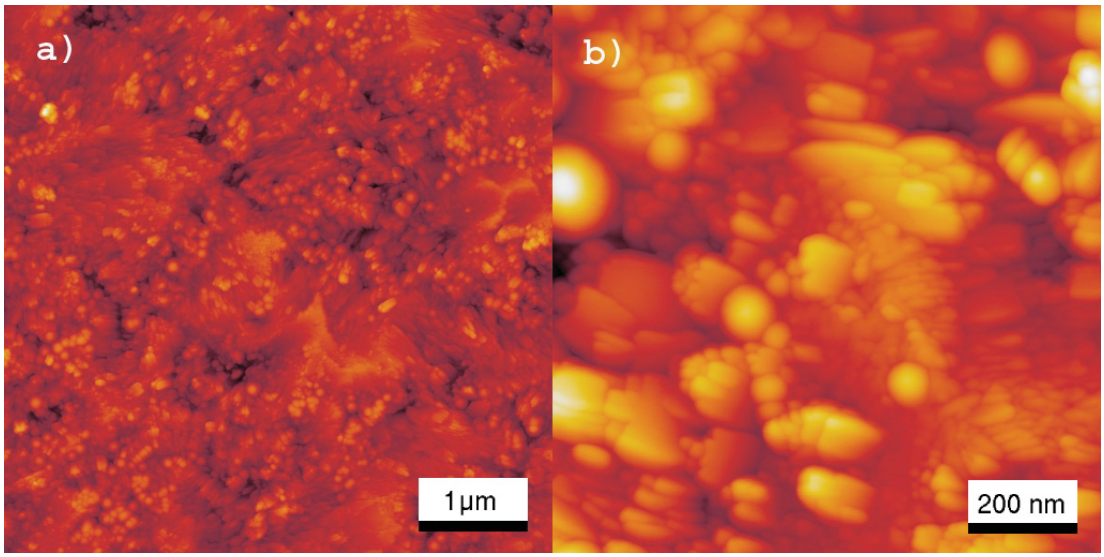

Fig. 17: Topography of V_2O_5 on MgO (100); deposition temperature 100°C, z-scale: a) 150 nm, b) 75 nm

The sample produced at 100°C exhibits crystalline growth, plate like structures start to appear (see Fig. 17) The RMS value σ is found to be 11.0 ± 1 nm. At a deposition temperature of 150°C the morphology of the films is dominated by platelets that are about 150 x 150 x 40 nm in size (see Fig. 18 and Fig. 19). The RMS value has increased to 16.0 ± 1 nm.

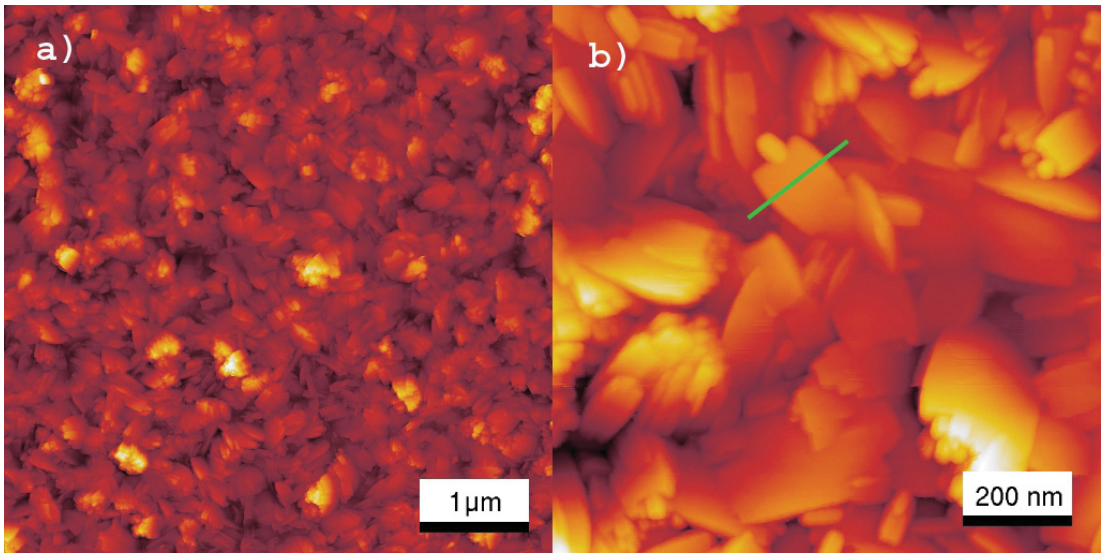

Fig. 18: Topography of V_2O_5 on MgO (100); deposition temperature 150°C, z-scale: a) 150 nm, b) 75 nm

The film deposited at 230°C exhibits well-defined platelets (see Fig. 20 and Fig. 21) that seem to increase in size with rising deposition temperature, which is in good agreement with the observed development of RMS roughness values with deposition temperature (see Fig. 24). The RMS value calculated for this film was found to be 17.0 ± 1 nm.

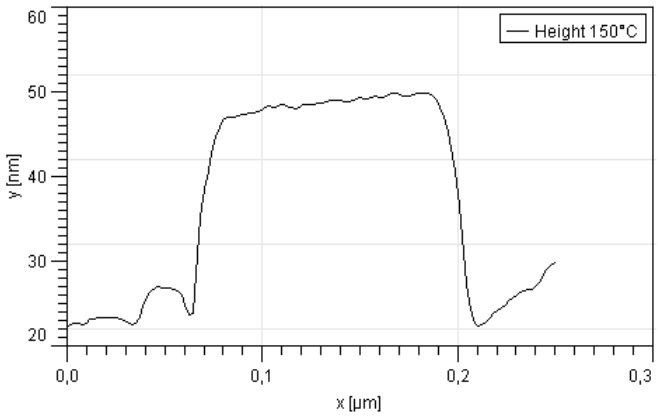

Fig. 19: Cross section of platelet indicated in Fig. 18b)

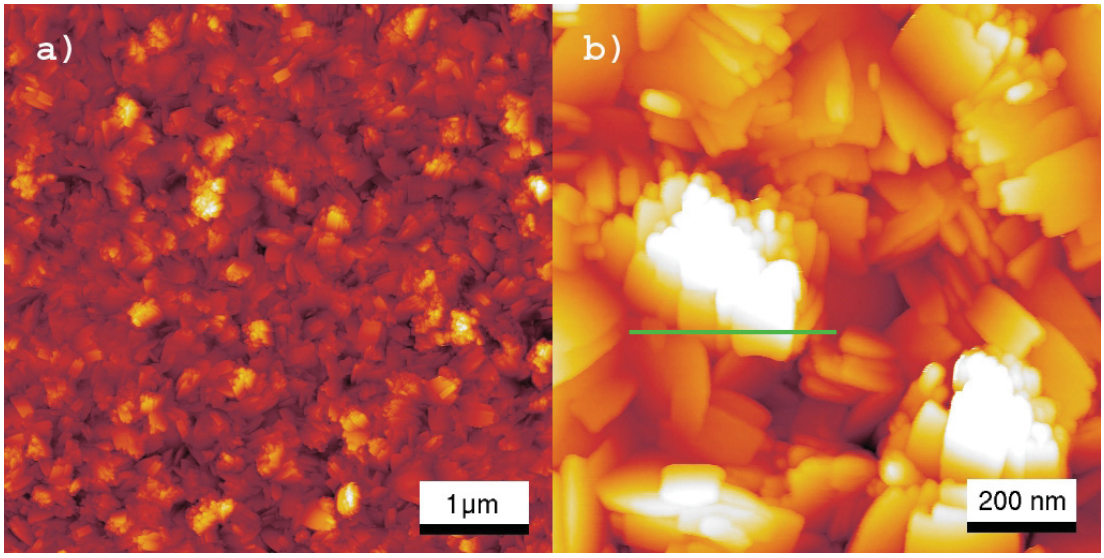

Fig. 20: Topography of V_2O_5 on MgO (100); deposition temperature 230°C, z-scale: a) 150 nm, b) 75 nm

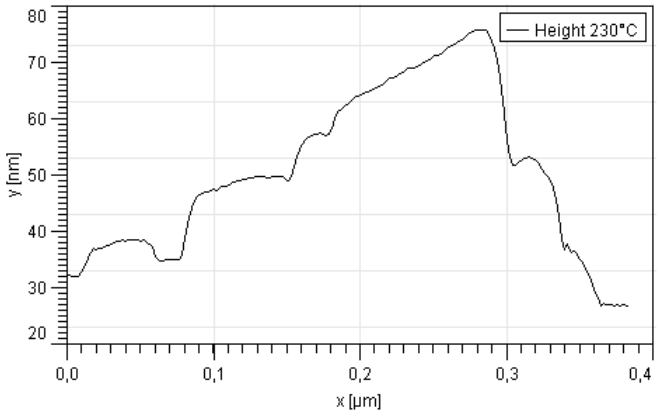

Fig. 21: Cross section of platelet as indicated in Fig. 20b)

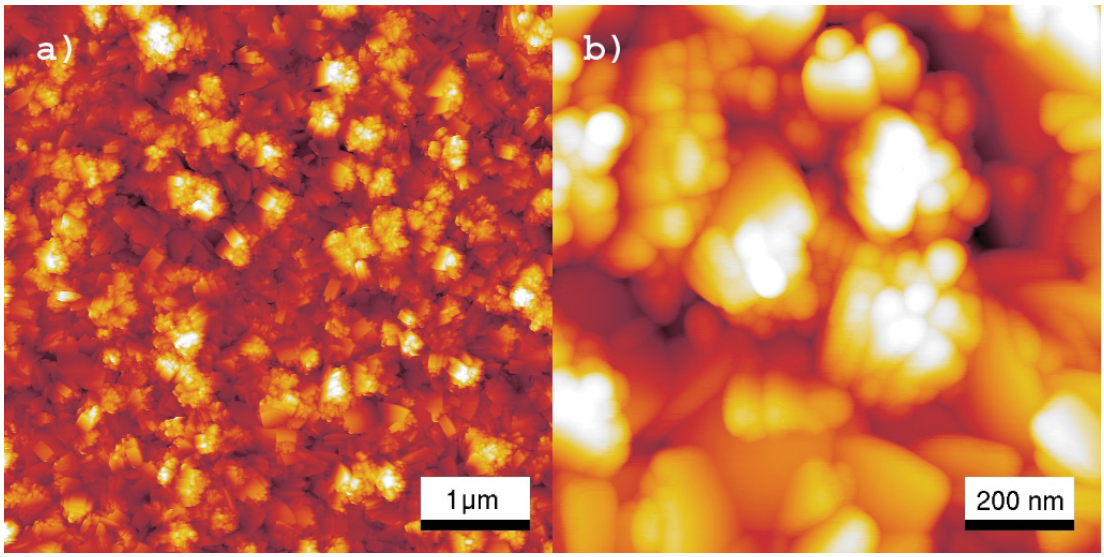

Fig. 22: Topography of V_2O_5 on MgO (100); deposition temperature 300°C, z-scale: a) 150 nm, b) 75 nm

No major change in topography in respect to sample deposited at 230°C is encountered looking at the sample produced at 300°C (see Fig. 22).

The HHCF was calculated from 5 x 5 µm images. In the case of the samples prepared at room temperature and 80°C a smaller area to calculate ξ and h had to be used as discussed later. The first data point of the HHCF of the investigated films was considered equal to the square of the RMS roughness parameter σ and treated as a constant in Eq. (26) when fitting the other parameters ξ an h. Fig. 23 shows an example of fitting of the HHCF calculated by the Gwyddion software package.

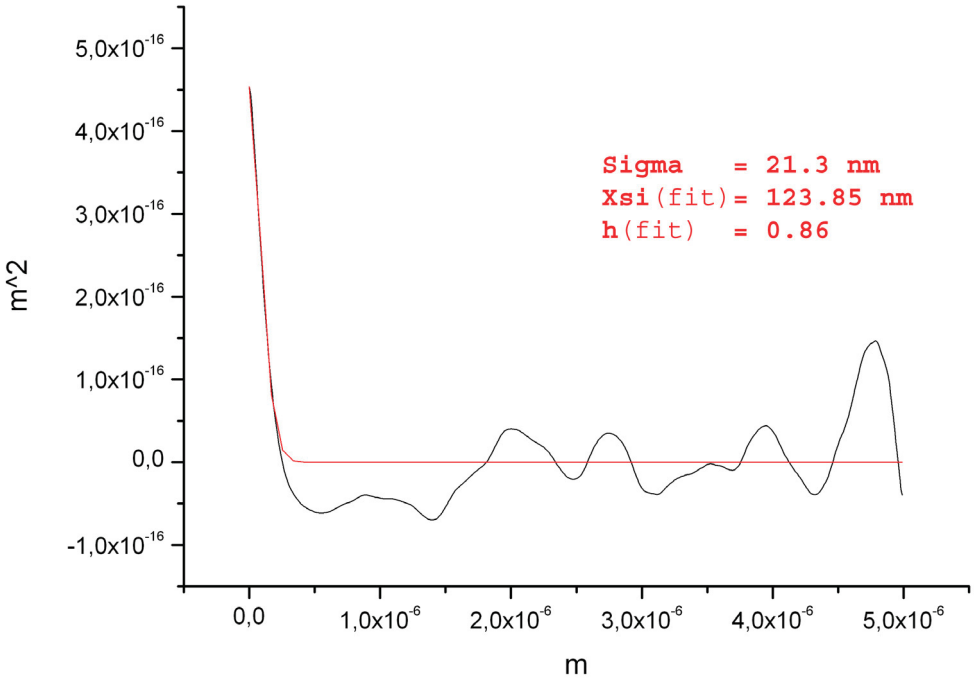

Fig. 23: HHCF of a V_2O_5 film deposited at 300°C fitted by Eq. (26)

The RMS value σ varies from 0.7 nm at room temperature to 21 nm at 300°C. The lines in Fig. 24 are guides for the eyes that indicate the transition from amorphous to crystalline growth and promoted grain growth with rising deposition temperatures. The RMS value was calculated twice for the film deposited at 80°C: The pits found were filtered by a height threshold to find σ without the pits to be 2.4 nm indicated by the gray data point, σ with the pits on the other hand was as high as 10 nm.

Fig. 22 shows the evolution of the lateral correlation length ξ. It exhibits a discontinuity at the crystallization onset temperature of 80°C. Since the HHCF needs to be calculated from a rectangular surface portion, filtering of the complex shaped pits cannot be done using a height threshold mask. The HHCF from which the values of ξ and h were calculated is derived from approximately 1.5 x 1.5 μm surface portions between the pits. The decreased number of data points casts doubt on the values calculated in this manner but unfortunately their acquisition was not possible otherwise.

The choosing of rectangular regions between the pits to calculate HHCF was found to be inappropriate for the room temperature sample since the spacing of surface contaminations was too narrow to allow for the collecting of data sets with any statistical value. The values for ξ and h were therefore calculated from the images including the surface contaminations. The discussed data points are gray in the respective plots.

The increase in RMS roughness from 0.7 nm at room temperature to 21 nm at 300°C can be attributed to the onset of crystalline growth at 80°C and the increase in crystallinity with rising deposition temperature [17]. Analog considerations can be undertaken regarding the increase in the lateral correlation length ξ that increases from 74 nm at room temperature to 122 nm at 300°C. The value of the hurst parameter h changes from 0.52 to 0.84 in the mentioned temperature interval, which can be connected to a less jagged surface morphology at higher temperatures.

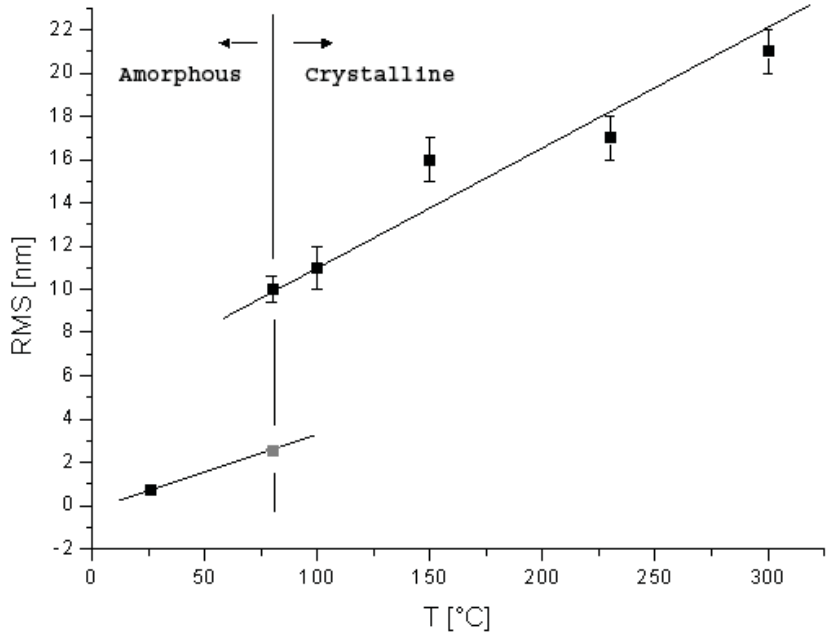

Fig. 24: RMS roughness versus deposition temperature of V_2O_5 thin films

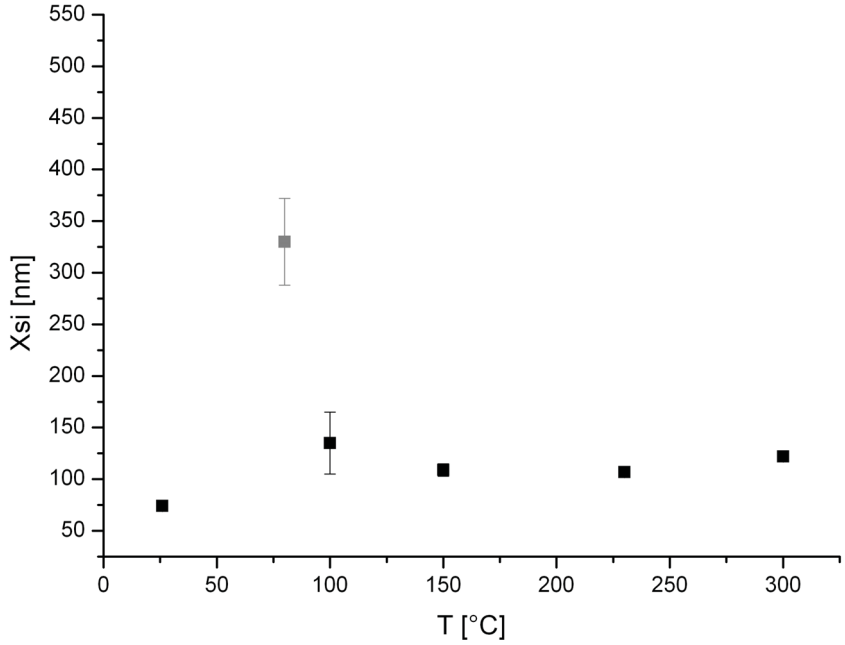

Fig. 25: Correlation length versus deposition temperature of V_2O_5 thin films

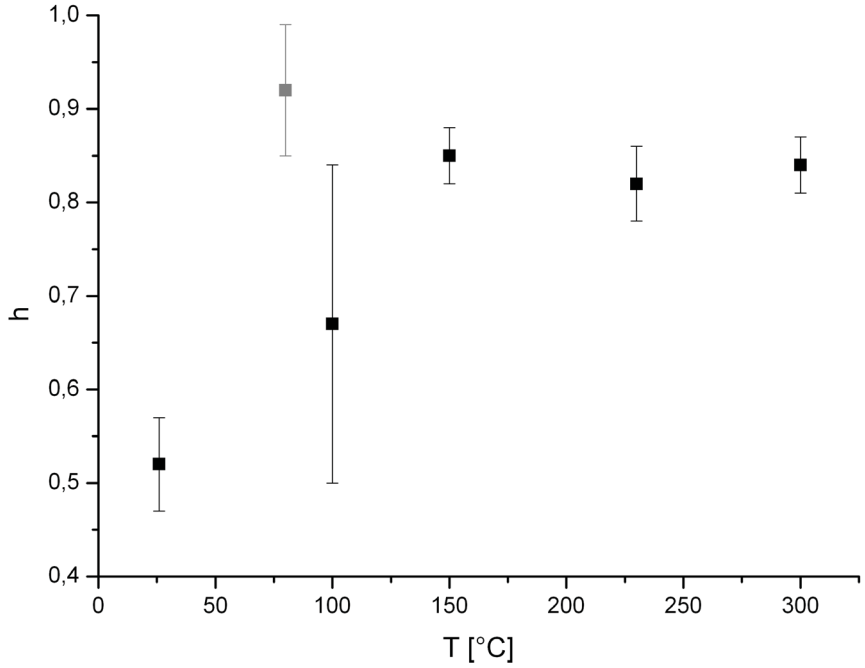

Fig. 26: Hurst parameter versus deposition temperature of V_2O_5 thin films

Fig. 27 shows the topography of V_2O_5 on Si(100) deposited at 300°C by dc reactive magnetron sputtering. Fig. 29 shows the topography of V_2O_5 on Si(100) deposited at 300°C by pulsed dc reactive magnetron sputtering. On these two samples friction force measurements were conducted since the ones on MgO(100) were not available at the time this work was conducted. Tab. 1 shows the roughness parameters of the films.

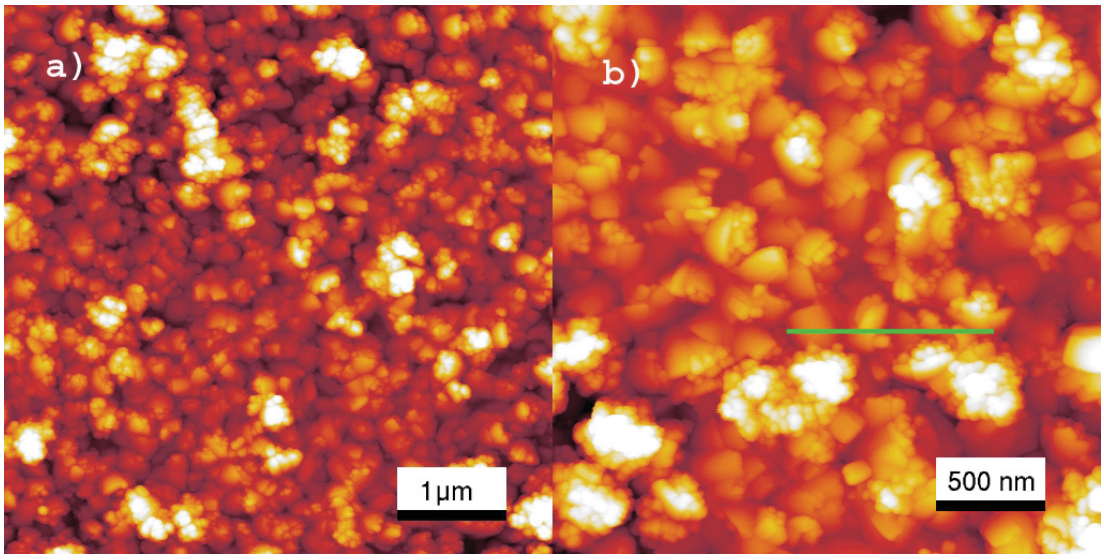

Fig. 27: TM-AFM images of V_2O_5 on Si (100) deposited at 300°C, z-scale: a) 100 nm, b) 50 nm

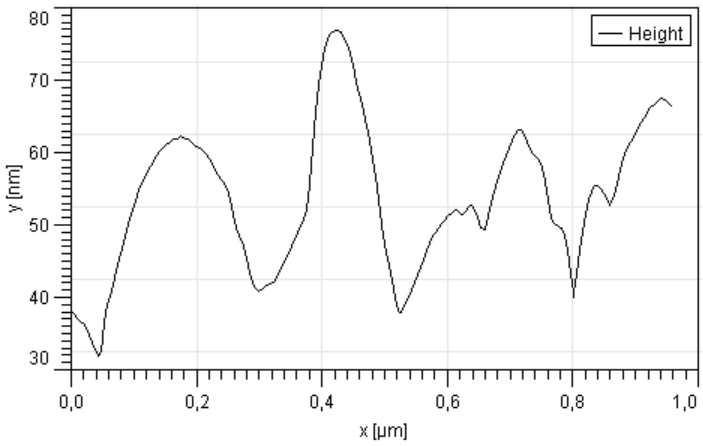

Fig. 28: Cross section as indicated in Fig. 27b)

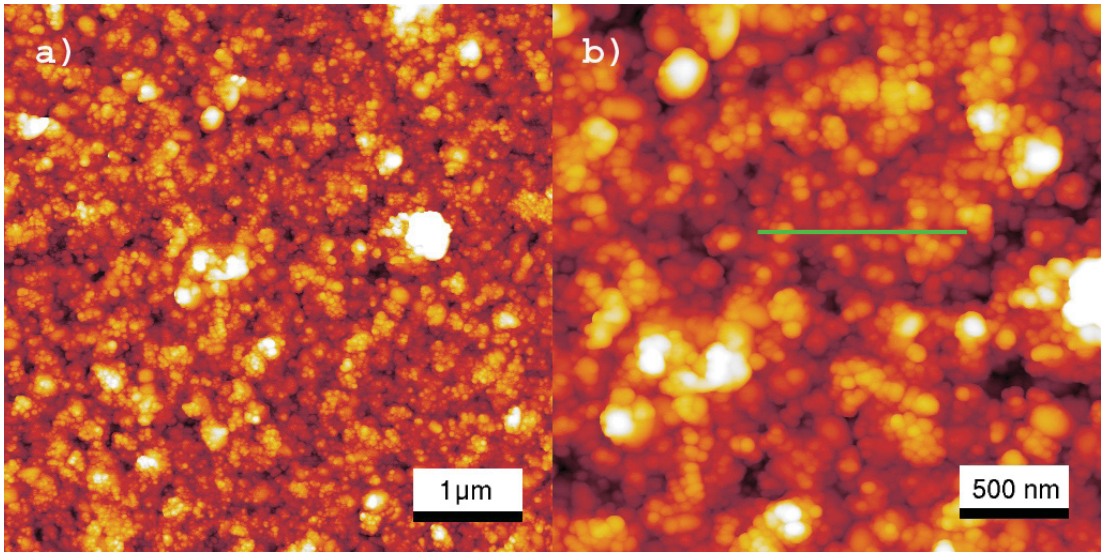

Fig. 29: TM-AFM images of V_2O_5 on Si (100) deposited at 300°C, z-scale 100 nm in a) and b)

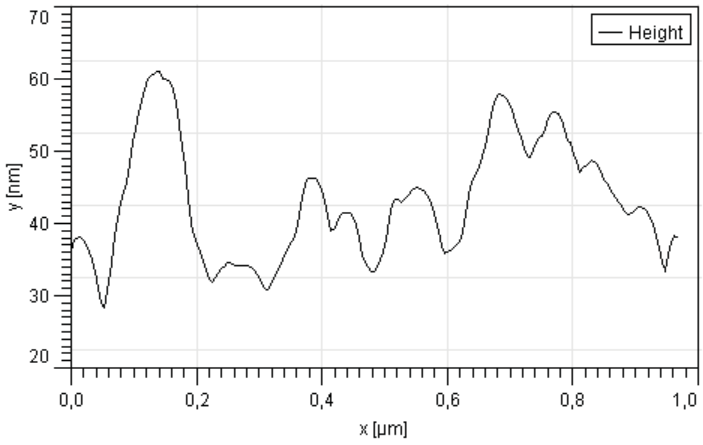

Fig. 30: Cross section as indicated in Fig. 29b)

	σ [nm]	ξ [nm]	h
DC magnetron sputtering	19 ±1	157 ±20	0,78 ±0,13
Pulsed DC magnetron sputtering	16 ±1	119 ±25	0,64 ±0,11

Tab. 1: Roughness parameters of V_2O_5 films deposited at 300°C

The smaller lateral correlation length ξ and hurst parameter h of the film prepared by pulsed dc reactive magnetron sputtering can be related to the smaller surface features that the film exhibits (compare Fig. 28 and Fig. 30). XRD measurements show that both films are of polycrystalline nature. The film deposited via dc reactive magnetron sputtering shows a preferred (200) orientation whereas for the one prepared by pulsed dc reactive magnetron sputtering the intensities of the (001) and (110) reflections are almost equal [19].

3.1.2 TiN and TiN/Ag nanocomposite films

The morphology of films of pure TiN (see Fig. 31 and Fig. 32) and TiN coatings with two different Ag contents, approximately 7 at.% Ag (see Fig. 33 and Fig. 35) and 45 at.% Ag (see Fig. 37), were investigated. The values of σ, ξ and h can be found in Tab. 2 as well as the median surface feature radii r_i that were determined via a watershed algorithm (see 1.7). Fig. 34 shows an example of the surface feature radius distribution of TiN with 7 at.% Ag.

TiN with	σ [nm]	ξ [nm]	h	ri [nm]
7% Ag	4.7 ±0.2	60 ±4	0.95 ±0.3	50 ±20
45% Ag	7.6 ±0.6	54 ±5	1.00 ±0.005	30 ±20
Pure TiN	2,4 ±0,1	72 ±5	0.74 ±0.05	

Tab. 2: Roughness parameters and mean feature radii of TiN and TiN/Ag films

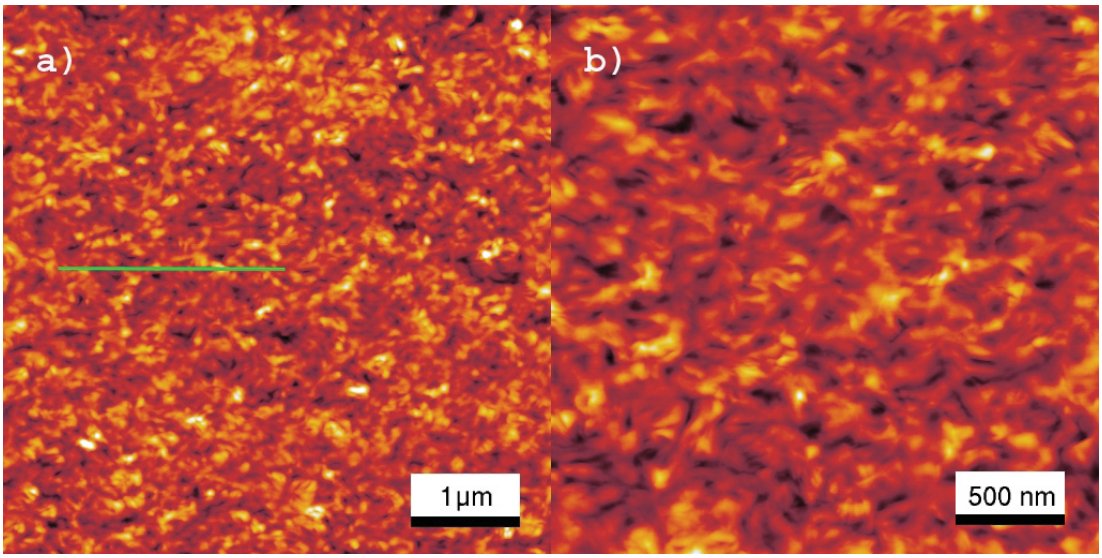

Fig. 31: TM-AFM images of pure TiN on Si(100) deposited at 550°C, z-scale in a) and b) 20 nm

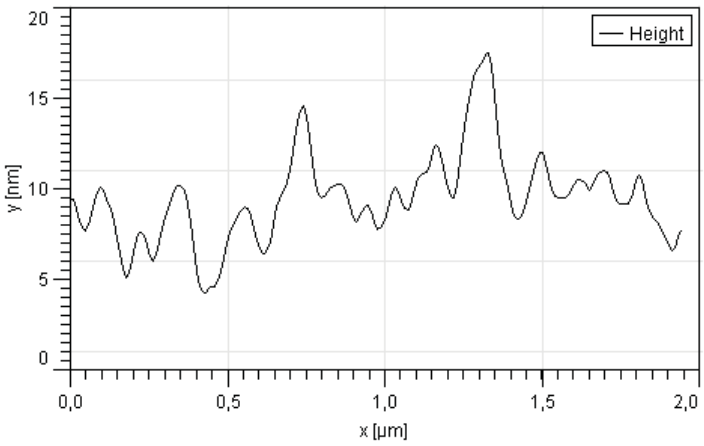

Fig. 32: Cross section of TiN on Si(100) as indicated in Fig. 31

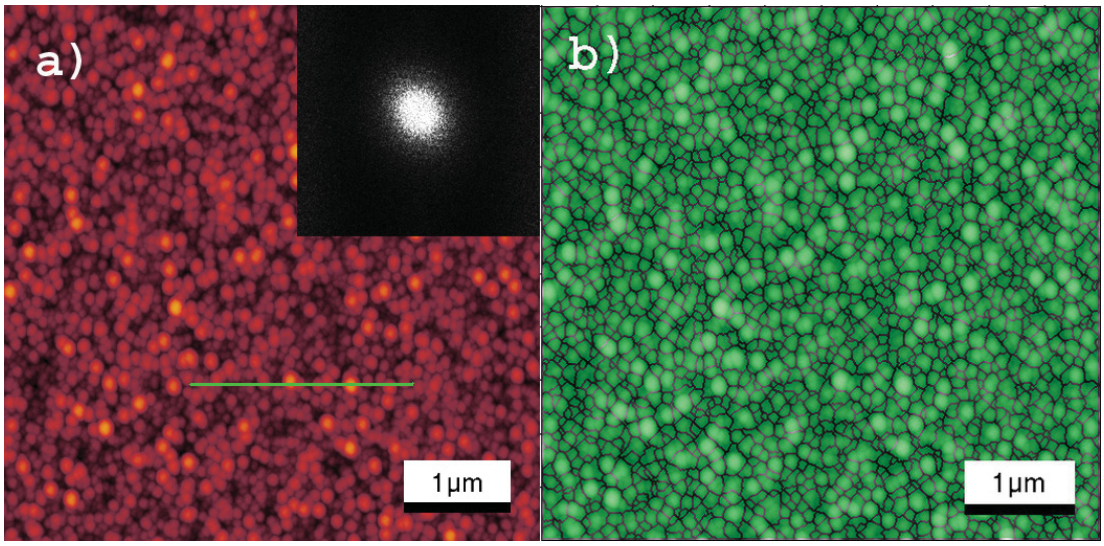

Fig. 33: a) TM-AFM image of TiN with 7 at.% Ag on Si(100), inset in a) FFT from -50 μm^{-1} to 50 μm^{-1}, z-scale: a) 50 nm, b) watershed analysis mask of the same image

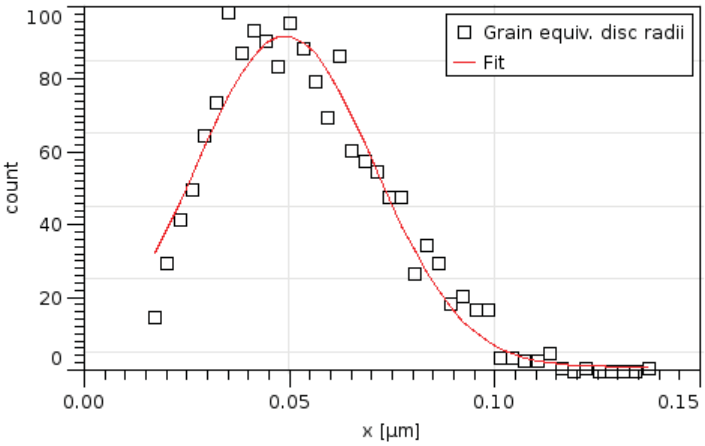

Fig. 34: Plot of surface feature equivalent disc radii: TiN on Si(100) with 7 at.% Ag

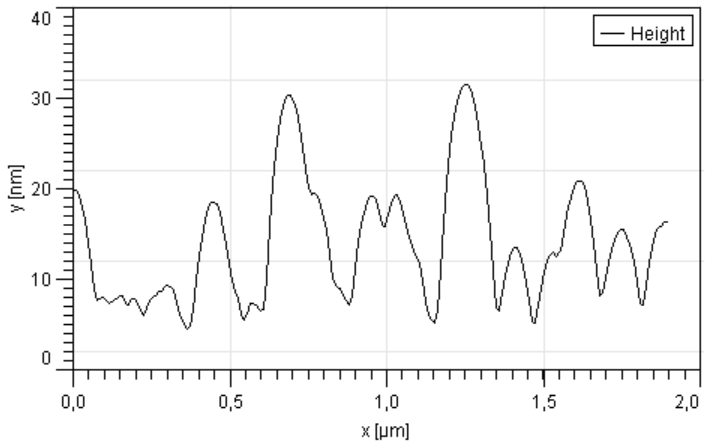

Fig. 35: Cross section of TiN on Si(100) with 7 at.% Ag as indicated in Fig. 33a)

Fig. 36 shows the radial power spectral density function (radial PSDF) calculated from Fig. 33a). It exhibits a slight peak that can be linked to a preferential surface feature separation of 180 nm in real space.

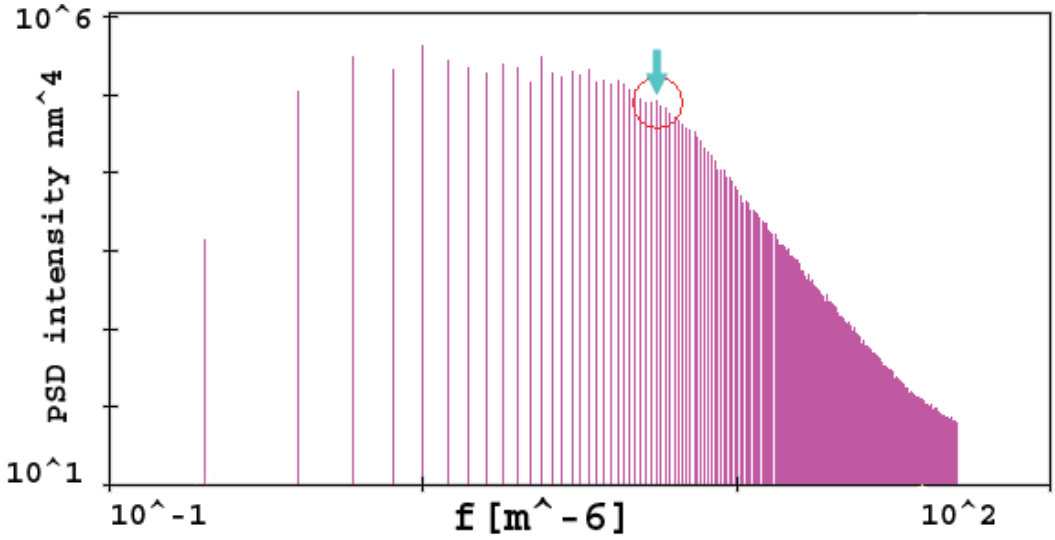

Fig. 36: Radial power spectral density function of Ag Fig. 33a) TiN with 7 at.%

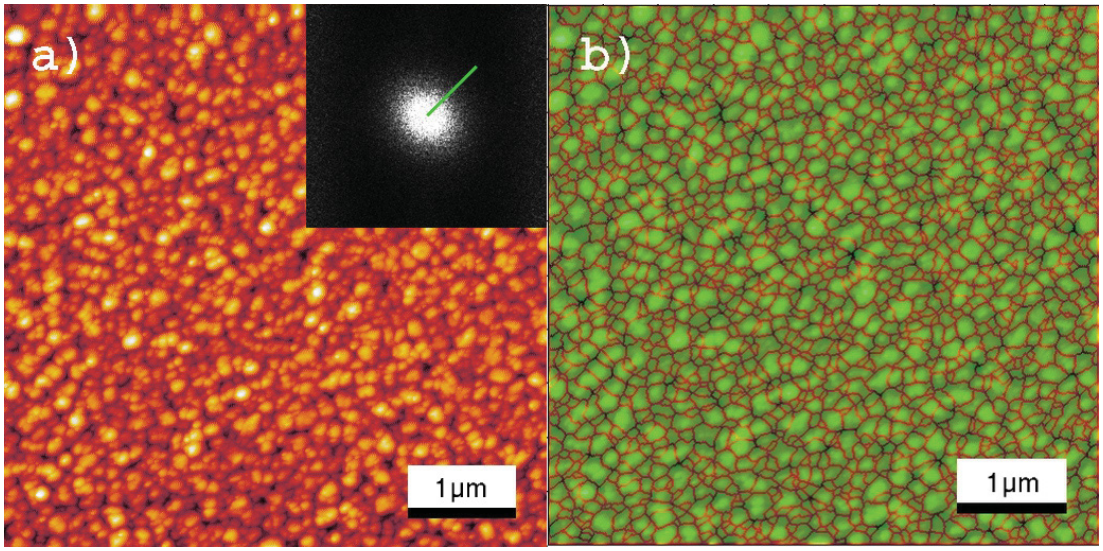

Fig. 37: a) TM-AFM image of TiN with 45 at.% Ag on Si(100), inset in a) FFT from -50 μm^{-1} to 50 μm^{-1}, z-scale: a) 50 nm, b) watershed analysis mask of the same image

The film containing 45 at.% Ag exhibits higher σ and lower ξ values than the one with 7 at.% Ag, the lateral feature size is slightly smaller. This corresponds well with SEM images of the films [20]. The radial PSDF calculated from Fig. 37a) shows a slight peak which yields information on the preferential separation of the prominent surface features of about 250 nm (see Fig. 38). The inset in Fig. 37a) displays the fast Fourier transformation (FFT) of the image. The cross section of the FFT in a random direction exhibits a slight ring (see Fig. 39). The ring's position also yields information on the preferential separation of the prominent surface features. Its value of 240 nm corresponds well with the value found analysing the radial PDSF calculated from Fig. 37a). More detail of the film's morphology is shown in Fig. 40 and its cross section (see Fig. 41).

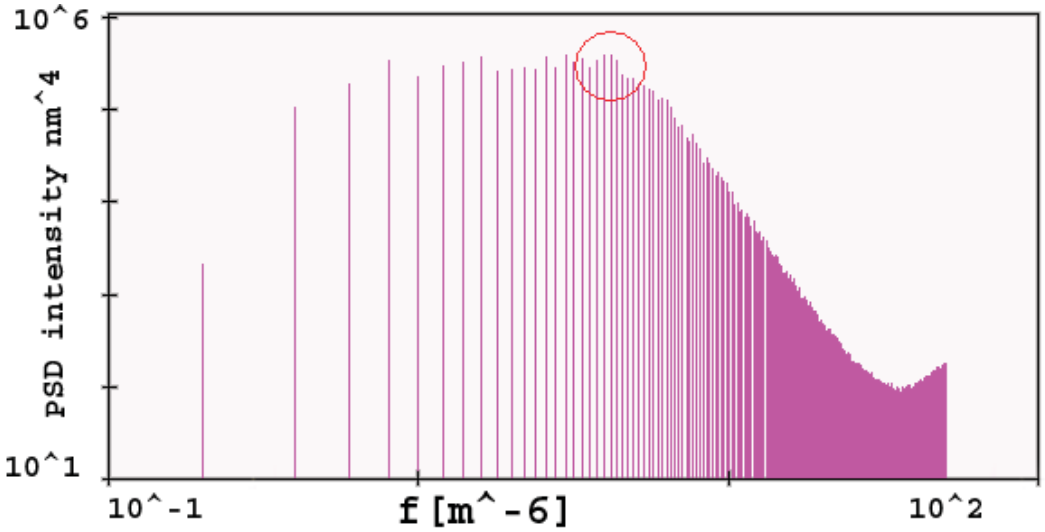

Fig. 38: Radial power spectral density function of Fig. 37a): TiN with 45 at.% Ag

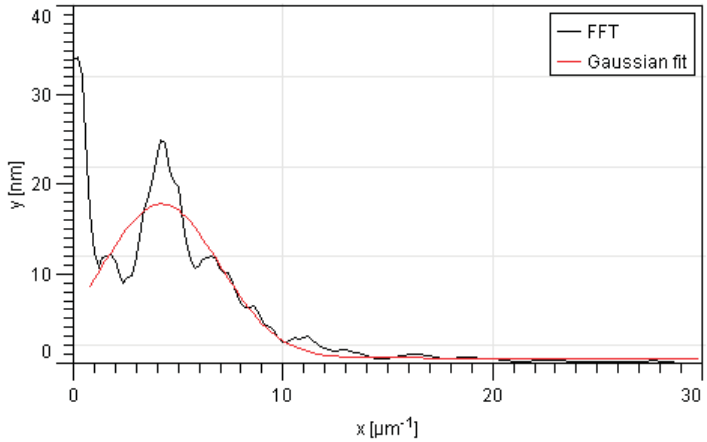

Fig. 39: Cross section of FFT as indicated in inset of Fig. 37a)

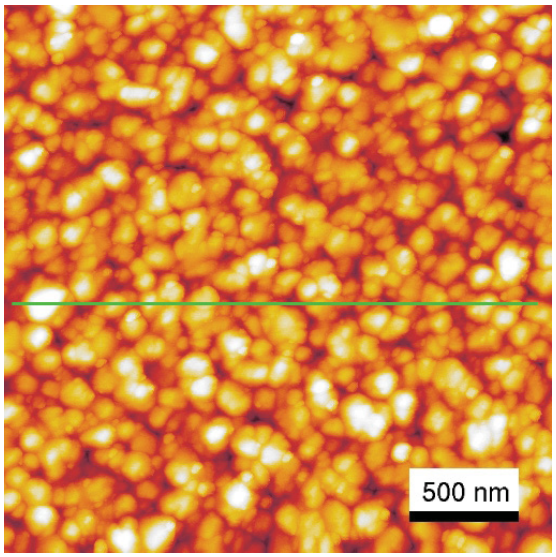

Fig. 40: TM-AFM image of TiN with 45 at.% Ag, z-scale: 50 nm

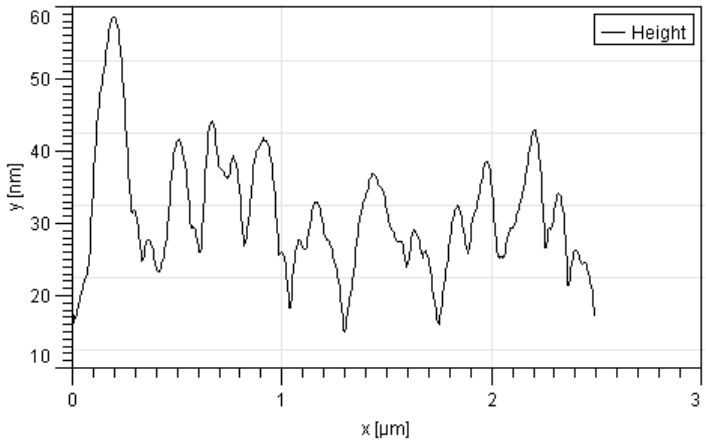

Fig. 41: Cross section as indicated in Fig. 40

3.2 Implementation of Varenberg method on mica, Au and SiO_2

For first tests of Varenberg's method, a flat surface was thought to be appropriate. Therefore freshly cleaved mica was chosen. The RMS roughness σ was 0.1 nm, calculated from 5 x 5 µm images. All the measurements on mica were performed at L = 50 nN. As seen in Tab. 3 a slight speed dependence of the friction coefficient could be observed. Descriptions of the dependence of scan speed on friction forces found in the literature are contradictory. Friction coefficients were found to increase [22] and decrease [23] with rising scan speed or not to change at all [24]. Since nanoscale friction can be a function of the atmosphere's relative humidity (RH) [25] all measurements on mica were performed at 45% RH and therefore should not be influenced by a change in the same. A possible influence of sample orientation [24] was not investigated,

scanning in the same orientation during all the measurements. Detailed results are found in appendix 7.1.2.

Scan size [nm]	Tip speed [µm/s]	Friction coeffiecient µ
100 x 100	0.4	0.03 ±0.01
500 x 500	1	0.03 ±0.01
1000 x 1000	2	0.07 ±0.02
1000 x 1000	4	0.16 ±0.02

Tab. 3: Friction coefficients on mica at various tip speeds

Results for friction coefficients found on Au(111) (σ = 2 nm, calculated from 5 x 5 µm images) are shown in Tab. 4. Also see appendix 7.1.3.

Scan size [nm]	Tip speed [µm/s]	Friction coeffiecient µ
100 x 100	0.4	0.05 ±0.01
1000 x 1000	2	0.07 ±0.03

Tab. 4: Friction coefficients on Au(111) at various tip speeds

The determined friction coefficient values for mica and Au are comparable to those found in the literature, being 0.03 for mica [29] and 0.08 for Au [23]. Other groups found no speed dependence of µ on Au [23]. On SiO_2 (TGF11), the value of $\mu = 0.32 \pm 0.02$ is in good agreement with those found by Varenberg [9] and the ones determined by the tip calibration procedure deriving from Eq. (21) - see appendix 7.1.1.

3.3 Friction coefficients on Low Friction Coatings

3.3.1 V_2O_5 thin films

On samples of V_2O_5 the friction coefficients μ_i were determined using tip speeds of 2 µm/s and 0.4 µm/s. Scan sizes were 1x1 µm and 100 x 100 nm respectively. The loads applied ranged from 50 to 125 nN (see appendix 7.1.2). Fig. 42a) shows the topography and Fig. 42b) the "trace minus retrace" image (see 1.7) of deflection of V_2O_5 prepared using dc reactive magnetron sputtering. In Fig. 42b) topography induced artefacts can be observed. After filtering of these artifacts the mean value of deflection in these "trace minus retrace" images was calculated to finally determine the friction coefficients.

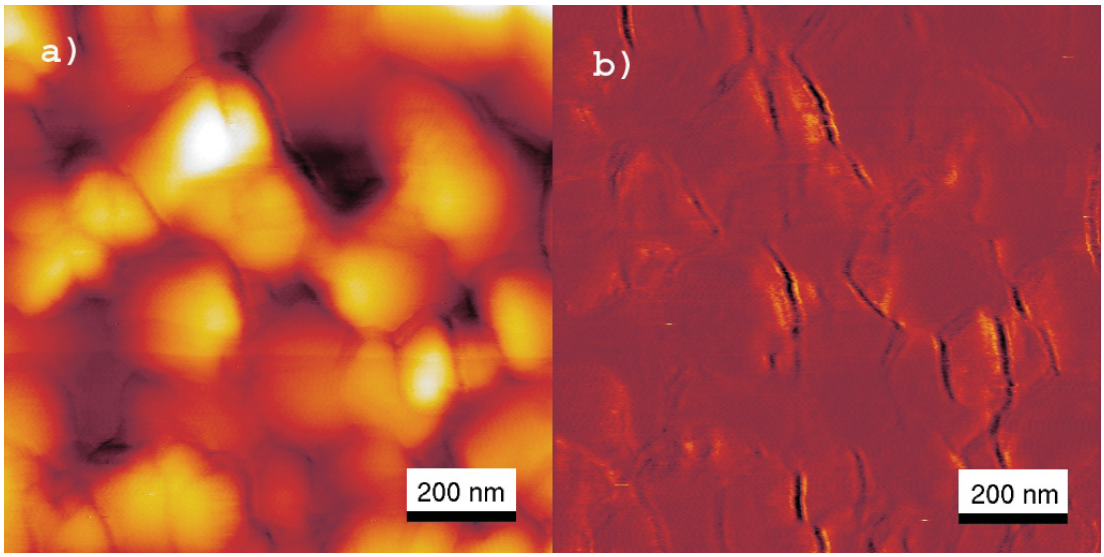

Fig. 42: a) Topography of V_2O_5 on Si (100), b) corresponding FFM "trace minus retrace" image, z sacle: a) 50 nm, b) 2 V

On the sample prepared via dc reactive magnetron sputtering the values of μ are 0.12 ± 0.03 at 2 μm/s and 0.10 ± 0.03 at 0.4 μm/s; a value of μ for V_2O_5 found in the literature is 0.17 [26].

Fig. 43 shows an equivalent image for a sample of V_2O_5 produced using pulsed dc reactive magnetron sputtering. The values of μ are found to be 0.11 ± 0.01 at 2 μm/s, 0.09 ± 0.01 at 1 μm/s and 0.05 ± 0.01 at 0.4 μm/s.

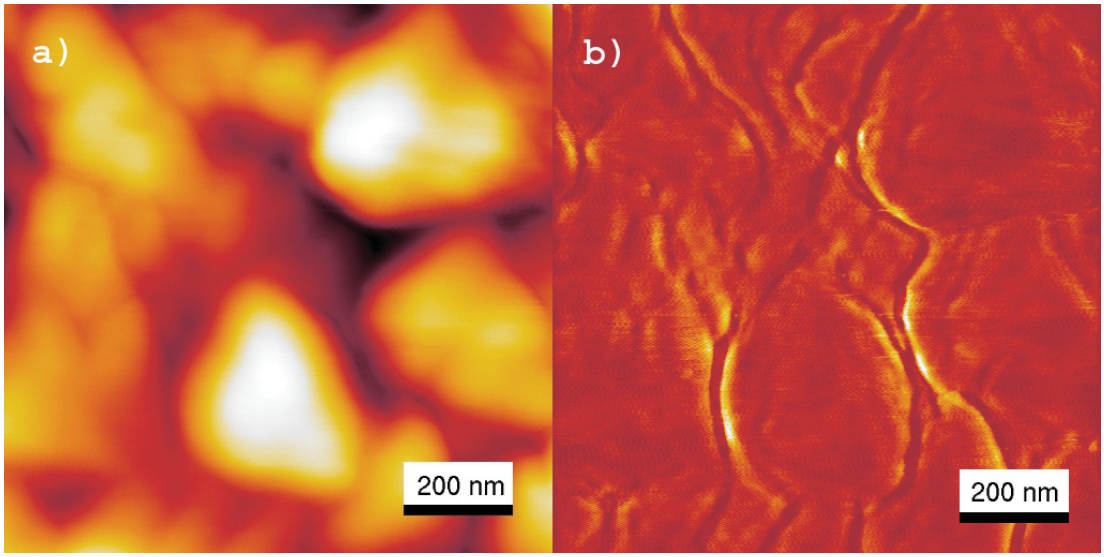

Fig. 43: a) Topography of V_2O_5 on Si (100), b) corresponding FFM "trace minus retrace" image, z-scale: a) 50 nm, b) 0.7 V

Since the film grown using pulsed dc reactive magnetron sputtering has a different preferred growth orientation, a difference in friction coefficient would have been understandable. No significant difference was found at a scan speed of 2 μm/s. Other groups found no influence of preferred orientation of growth of V_2O_5 thin films on macroscopic friction [27]. Detailed results are found in appendices 7.1.4 and 7.1.5.

3.3.2 TiN and TiN/Ag nanocomposite films

The same procedure as described for V_2O_5 involving filtering of topography induced artefacts in the "trace minus retrace image" of an FFM scan was applied for the systems pure TiN and TiN with Ag. Films of pure TiN (see Fig. 44) and TiN with 7at.% Ag (see Fig. 45) were investigated. Scan speeds were 2 µm/s and 0.4 µm/s. Scan sizes were 1x1 µm and 100 x 100 nm respectively.

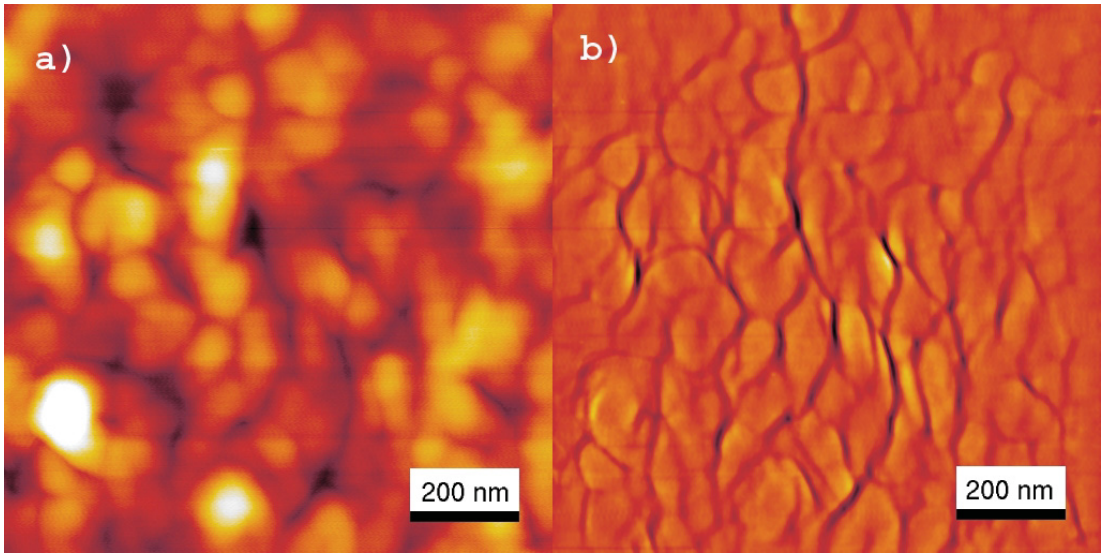

Fig. 44: a) Topography of pure TiN on Si (100), b) corresponding FFM "trace minus retrace" image, z-scale: a) 50 nm, b) 1 V

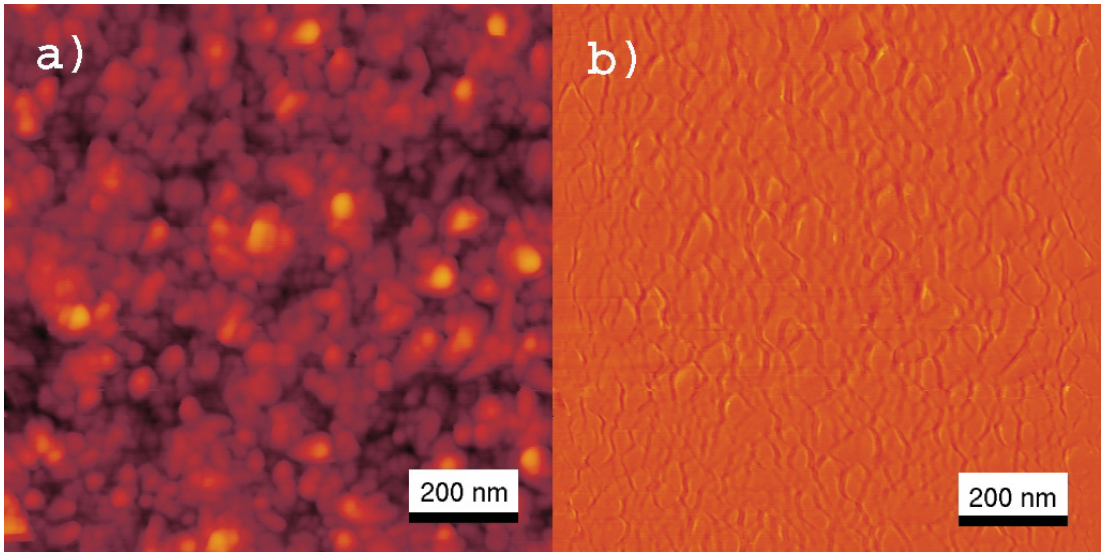

Fig. 45: a) Topography of TiN with 7 at.% Ag on Si (100), b) corresponding FFM "trace minus retrace" image, z sacle: a) 50 nm, b) 2 V

The µ value of 0.06 ± 0.02 for pure TiN and 0.07 ± 0.01 for the TiN film with 7%Ag was found to be equal for both speeds. The value for pure TiN found in the literature is 0.104 ± 0.017 [29]. The loads applied ranged from 50 to 110 nN - see appendices 7.1.6 and 7.1.7.

4 Discussion

4.1 Gain dependence of lateral deflection

Lateral deflection was found to be dependent on gains imposed by the operator. Investigating mica samples using very low gains of about 0.1 to 1 for the integral gain (IG) and 1 to 10 for the proportional gain (PG) levels of lateral deflection occurred that lead to the calculation of friction coefficients above 1 that were therefore considered dubious. Increasing gains to about 4 for the IG and 40 for the PG, a sudden drop in the level of lateral deflection was observed (see Fig. 46). The friction coefficients calculated from the low level data were in very good agreement with data found by other groups cited in the *Results* section of this work. Another factor that favors choosing higher gains is the fact that trace and retrace are overlapping more closely with the higher gains. Unfortunately it was not possible to come up with a rule of thumb for the necessary gain values. The mentioned transition occurs at different gain settings investigating different morphologies. They seem to depend on surface roughness and applied force; seemingly they are higher when applying more force to the surface. A quiet working environment without any sources of vibration is beneficial as in every AFM technique. Within this work the author did not succeed in recording friction force images that were completely free of noise. Since the average values of deflection were of interest, this noise should not have too much influence on the accuracy of friction coefficient values.

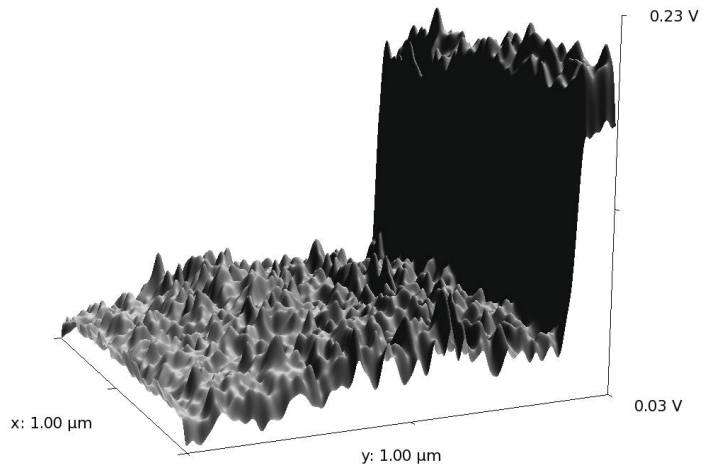

Fig. 46: Trace minus retrace image: Occurrence of a higher level of lateral deflection due to use of too low gains (right part of the image)

4.2 Occurrence of double tips

The measurements were performed using four calibrated cantilevers. Due to heavy use one tip showed a change of its shape. Fig. 47 presents an image with unnatural triangular surface features. This is usually caused by a change of the tip's original geometry. The calibration factor of the cantilever was checked on TGF11 and was found to be unchanged. After comparing the friction force values acquired on the sample using this cantilever with the values of a freshly calibrated cantilever with a virgin tip they were found to be the same. Therefore, the author believes that the values recorded with this "bad" tip are trustworthy.

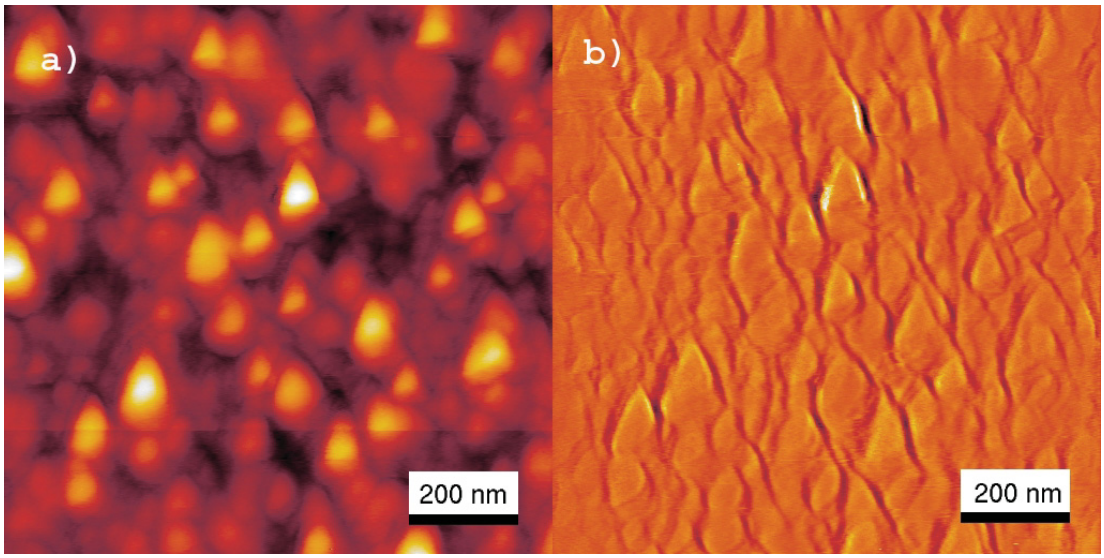

Fig. 47: a) Topography of TiN with 7 at.% Ag on Si (100), b) corresponding FFM "trace minus retrace" image, z sacle: a) 30 nm, b) 2 V

4.3 Possible cause of change in friction coefficients

According to Bhushan [30], a change in the relative velocity between the tip and the sample surface results in a change in the shear strain rate which generally influences the mechanical properties of the mating materials. High sliding speeds can give rise to high interface temperatures that can significantly reduce material strength, which leads to a higher area of contact resulting in a higher coefficient of friction.

Note that on polished quartz surfaces at loads below 20 nN, friction forces were found to be non-linear due to a transition from macro style friction to single asperity contact friction [28]. In the present work values of load were chosen well above the mentioned level. Therfore, no

significant changes in friction coefficients with variations in applied load were observed.

Other groups found the friction coefficient to depend on tip radius [25]. Investigating mica samples with Si_3N_4 tips, other authors found that the tip apex can be modified during friction scans if the applied load is sufficiently high - in the order of 350 nN [24]. This possible influence on friction coefficients was not investigated in the present work.

5 Summary and outlook

The morphology of the low friction coating systems V_2O_5 on Si(100) and MgO(100) as well as pure TiN and TiN-Ag nanocomposites on Si(100) fabricated by unbalanced dc reactive magnetron sputtering was investigated using Atomic Force Microscopy (AFM). Tapping mode AFM was utilized to acquire quantitative data describing the surface roughness. Analysing the height-height-correlation function, the evolution of the surface roughness parameters root mean square roughness (RMS or σ), lateral correlation length ξ and the hurst parameter h was investigated.

Studying samples of V_2O_5 on MgO(100) deposited at temperatures from 26°C to 300°C, a transition from amorphous to crystalline growth at 80°C was observed that goes hand in hand with a significant increase in RMS roughness. The σ value rises from 0.7 nm at 26°C to 21 nm at 300°C. The film fabricated at the transition temperature exhibits pits of about 50 nm in depth that harbor little surface features of approximately 50 to 100 nm in diameter. Above 80°C, the film morphology is dominated by little platelets of about 150 x 150 x 40 nm in size. Film crystallinity increases with rising deposition temperature.

Roughness parameters of V_2O_5 on Si(100) deposited at 300°C were found to be different when comparing the films prepared by dc reactive magnetron sputtering and pulsed dc reactive magnetron sputtering. In the first case ξ and h are slightly higher than on the film prepared by pulsed dc reactive magnetron sputtering. This can be explained by the smaller surface features that this film exhibits; no distinct platelets could be found on the film fabricated using pulsed dc reactive magnetron sputtering. The values of σ of the two films were found to be comparable.

Further, the morphology of films of pure TiN, TiN with approximately 7 at.% Ag and 45 at.% Ag was investigated. The film of pure TiN was produced at 550°C, the other two coatings at 150°C. In contrast to the samples containing Ag, the film of pure TiN was found to have lower values of σ and h but a higher value of ξ. Comparing the TiN-Ag nanocomposite films, a slightly higher value of σ and a smaller average surface feature diameter were obtained in the sample with 45 at.% Ag. Analysing the radial power spectral density function, a preferential surface feature separation of about 180 nm was determined for the film with 7 at.% Ag. On TiN with 45 at.% Ag this distance was 250 nm.

Finally, a method to quantitatively determine coefficients of friction via Friction Force Microscopy (FFM) has been implemented. Recording the thermal spectrum from the unloaded cantilever excited to oscillate by Brownian motion the value of the cantilever's spring constant was acquired. Thus it was possible to calculate the values of the surface contact forces. The calibration factor α [N/V] that directly links lateral deflection in FFM with friction force was measured using a calibration grating of known geometry. On a reference sample of Mica(0001), coefficients of friction were observed to increase with scan speed from 0.03 ± 0.01 at 0.4 μm/s to 0.16 ± 0.02 at 4 μm/s; scan areas were 100 nm x 100 nm and 1 μm x 1 μm, respectively. The applied load on Mica was 50 nN.

At a scan speed of 2 μm/s, values of the friction coefficients on pure TiN and TiN with 7 at.% Ag were found to be 0.06± 0.02 and 0.07 ± 0.01, respectively. Applied loads in these measurements ranged from 50 to 110 nN.

Friction coefficients of V_2O_5 on Si(100) deposited at 300°C were found to show no significant difference when comparing the films prepared by dc reactive magnetron sputtering and pulsed dc reactive magnetron sputtering. At a scan speed of 2 μm/s they were found to be 0.12 ± 0.03 and 0.11 ± 0.01, respectively. Scanning with a speed of 0.4 μm/s the values were found to have decreased to 0.10 ± 0.03 and 0.05 ± 0.01, respectively. Applied loads during these measurements ranged from 50 to 125 nN.

Since contradictory information on the observed speed dependence of friction coefficients on mica was found in the literature [22-24], further research should be undertaken to clarify the reasons of this dependence. Other tip/sample material matches could be investigated. Temperature values influence the shear resistance of the sample and therefore the area of contact between the tip and the sample, which has an impact on friction coefficients. The load values at which wear on e.g. V_2O_5 starts to be of importance might be a question worth pursuing. Considering the dependence of friction coefficients on tip radii, a closer exploration of the thin film systems addressed in the present work using probes with varying apex radius might be another field of possible future research.

6 References

1. G.Binning, H. Rohrer, Helv. Phys. Acta **55** (1982) 726.
2. G. Binning, K.F. Quate, C. Gerber, Phys. Rev. Lett. **56** (1986) 930-933.
3. G. Meyer, N. Amer, Appl. Phys. Lett. **53** (1988) 1045-1047.
4. http://www.farmfak.uu.se/farm/farmfyskem-web/instrumentation/images/afm.gif
5. http://www.ntmdt.com/SPM-Techniques/Principles/AFM/dc_Contact_techniques/Lateral_Force_Imaging_mode11.html
6. J. E. Sader, J. Chon, P. Mulvaney, Rev. Sci. Instrum. **70** (1999) 3967-3969.
7. John E. Sader, J. Appl. Phys. **84** (1998) 64.
8. http://www.ampc.ms.unimelb.edu.au/afm/calibration.html#normal
9. M. Varenberg, I. Etison, G. Halperin, Rev. Sci. Instrum. **74** (2003) 3362-3367.
10. H.A. Rothbart, "Mechanical Design Handbook", 2nd ed., McGraw-Hill, New York, 1996, p. 5.77.
11. http://www.spmtips.com/tgf/
12. http://gwyddion.net
13. C. Teichert, Physics Reports 365 (2002), 225-432
14. C. Teichert, Script to "Scanning Probe Techniques for the Characterization of Solid Surfaces", Leoben
15. http://www.nanosensors.com/
16. MikroMasch Eesti, Tallinn, Estonia
17. N. Fateh, G. Fontalvo, L. Cha, T. Klünsner, G. Hlawacek, C. Teichert, C. Mitterer, Surf. Coat. Technol. **202** (2008) 1551-1555.
18. N. Fateh, G. Fontalvo, G. Gassner, C. Mitterer, Tribol. Lett. **28** (2007) 1–7.
19. N. Fateh, G. Fontalvo, C. Mitterer, J. Phys. D: Appl. Phys. **40** (2007) 7716–7719.
20. H. Köstenbauer, G. A. Fontalvo, C. Mitterer, G. Hlawacek, C. Teichert, J. Keckes; J. Nanosci. Nanotechnol. In print, 2008
21. J. Thornton, J. Vac. Sci. Technol. **11** (1974) 666.
22. Y. Liu, T. Wu, and D.F. Evans, Langmuir **10** (1994) 2241.
23. N.V. Koinkar, B. Bhushan, J. Vac. Sci. Technol. A **14 (**1996) 2378-2391.
24. J. Hu, X. Xiao, D. Ogletree, M. Salmeron, Surf. Sci. **327** (1995) 358-370.
25. B. Bhushan, S. Sundararajan, Acta Mater **46** (1998) 3793-3804.
26. W. Gulbinski, T. Suszko, D. Pailharey, Wear **254** (2003) 988–993.
27. W. Gulbinski, T. Suszko, B. Warcholinski, W. Sienicki, Wear **254** (2003) 129–135.
28. M. Reitsma , R. Cain, S. Biggs, D. Smith, Appl. Surf. Sci. **252** (2006) 4964–4968.
29. D. Arias, D. Marulanda, A. Baena, A. Devia, Wear **261** (2006) 1232–1236.
30. B. Bhushan, Proceedings of the Seventh Leeds-Lyon Symposium on Tribology, Leeds, England, IPC Business Press, Guildford, UK, 1981, 39–44.

7 Appendix

7.1.1 Tip calibration results on TGF11

Tip # 22	k=0.1 N/m	μ (111)	μ (100)	α [N/V]
L [nN]	20	0,31	0,32	1,018E-07
A [nN]	5			
L [nN]	20	0.34	0.35	1.206E-07
A [nN]	5			
L [nN]	45	0,28	0,29	7,645E-08
A [nN]	3			
L [nN]	50	0,31	0,29	8,755E-08
A [nN]	8			
L [nN]	50	0.30	0.28	9.145E-08
A [nN]	10			
Mean		0,31	0,31	9,556E-08
Standard deviation		0.02	0.03	1.667E-08

Tip # 23	k=0.2 N/m	μ (111)	μ (100)	α [N/V]
L [nN]	40	0,31	0,32	1,811E-07
A [nN]	5			
L [nN]	40	0.32	0.32	1.862E-07
A [nN]	6			
L [nN]	100	0,28	0,26	1,583E-07
A [nN]	10			
L [nN]	100	0,33	0,26	1,815E-07
A [nN]	10			
L [nN]	100	0.32	0.29	1.872E-07
A [nN]	10			
Mean		0,31	0,29	1,788E-07
Standard deviation		0.02	0.03	1.182E-08

Tip # 24	k=0.2 N/m	μ (111)	μ (100)	α [N/V]
L [nN]	100	0.26	0.30	1.381E-07
A [nN]	5			
L [nN]	100	0,31	0,35	1,525E-07
A [nN]	5			
L [nN]	100	0,29	0,30	1,432E-07
A [nN]	10			
L [nN]	100	0.33	0.36	1.573E-07
A [nN]	10			
Mean		0,30	0,33	1,478E-07
Standard deviation		0.03	0.03	8,715E-09
After use on TiN/Ag and V2O5				
L [nN]	80	0.27	0.34	1.325E-07
A [nN]	15			
L [nN]	90	0,32	0,36	1,594E-07
A [nN]	20			

Tip # 26	k=0.2 N/m	μ (111)	μ (100)	α [N/V]
L [nN]	100	0.27	0.25	1.560E-07
A [nN]	20			
L [nN]	100	0,29	0,29	1,641E-07
A [nN]	20			
L [nN]	100	0,31	0,31	1,807E-07
A [nN]	20			
L [nN]	100	0.29	0.26	1.680E-07
A [nN]	20			
L [nN]	100	0,31	0,27	1,671E-07
A [nN]	20			
Mean		0,29	0,28	1,672E-07
Standard deviation		0.02	0.02	8.909E-09

7.1.2 *Quantitative FFM results of Mica(0001)*

Tip LFMR # 23	Scan size [nm]	100 x 100	100 x 100	100 x 100	100 x 100	100 x 100	100 x 100
	V tip [um/s]	0,4	0,4	0,4	0,4	0,4	0,4
	Δo/2 [V]	0,010	0,008	0,009	0,008	0,007	0,009
	Alpha [N/V]	1,79E-07	1,79E-07	1,79E-07	1,79E-07	1,79E-07	1,79E-07
	Fr	1,74E-09	1,50E-09	1,52E-09	1,50E-09	1,26E-09	1,56E-09
	Fn [N]	5,00E-08	5,00E-08	5,00E-08	5,00E-08	5,00E-08	5,00E-08
	μ	0,03	0,03	0,03	0,03	0,03	0,03

Tip LFMR # 23	Scan size [nm]	500 x 500	500 x 500	500 x 500	500 x 500	500 x 500	1000 x 1000
	V tip [um/s]	1	1	1	1	1	2
	Δo/2 [V]	0,007	0,011	0,009	0,009	0,009	0,018
	Alpha [N/V]	1,79E-07	1,79E-07	1,79E-07	1,79E-07	1,79E-07	1,79E-07
	Fr	1,16E-09	2,01E-09	1,64E-09	1,53E-09	1,54E-09	3,22E-09
	Fn [N]	5,00E-08	5,00E-08	5,00E-08	5,00E-08	5,00E-08	5,00E-08
	μ	0,02	0,04	0,03	0,03	0,03	0,06

Tip LFMR # 23	Scan size [nm]	1000 x 1000	1000 x 1000	1000 x 1000	1000 x 1000	1000 x 1000	1000 x 1000
	V tip [um/s]	2	2	2	2	2	2
	Δo/2 [V]	0,032	0,017	0,026	0,016	0,016	0,018
	Alpha [N/V]	1,79E-07	1,79E-07	1,79E-07	1,79E-07	1,79E-07	1,79E-07
	Fr	5,72E-09	2,99E-09	4,68E-09	2,88E-09	2,81E-09	3,13E-09
	Fn [N]	5,00E-08	5,00E-08	5,00E-08	5,00E-08	5,00E-08	5,00E-08
	μ	0,11	0,06	0,09	0,06	0,06	0,06

Tip LFMR # 23	Scan size [nm]	1000 x 1000	1000 x 1000	1000 x 1000	1000 x 1000	1000 x 1000	1000 x 1000
	V tip [um/s]	4	4	4	4	4	4
	Δo/2 [V]	0,037	0,039	0,046	0,045	0,049	0,050
	Alpha [N/V]	1,79E-07	1,79E-07	1,79E-07	1,79E-07	1,79E-07	1,79E-07
	Fr	6,62E-09	6,96E-09	8,22E-09	8,09E-09	8,75E-09	8,94E-09
	Fn [N]	5,00E-08	5,00E-08	5,00E-08	5,00E-08	5,00E-08	5,00E-08
	μ	0,13	0,14	0,16	0,16	0,18	0,18

7.1.3 *Quantitative FFM results of Au(111)*

Tip LFMR # 22	Scan size [nm]	1000 x 1000	1000 x 1000	1000 x 1000	100 x 100	100 x 100	100 x 100
	V tip [um/s]	2	2	2	0,4	0,4	0,4
	Δo/2 [V]	0,043	0,054	0,059	0,022	0,030	0,029
	Alpha [N/V]	9,56E-08	9,56E-08	9,56E-08	9,56E-08	9,56E-08	9,56E-08
	Fr	4,06E-09	5,16E-09	5,59E-09	2,11E-09	2,82E-09	2,78E-09
	Fn [N]	1,20E-07	1,30E-07	1,10E-07	5,00E-08	5,00E-08	1,10E-07
	μ	0,03	0,04	0,05	0,04	0,06	0,03

Tip LFMR # 23	Scan size [nm]	1000 x 1000	1000 x 1000	1000 x 1000	1000 x 1000	1000 x 1000
	V tip [um/s]	2	2	2	2	2
	Δo/2 [V]	0,035	0,025	0,019	0,023	0,026
	Alpha [N/V]	1,79E-07	1,79E-07	1,79E-07	1,79E-07	1,79E-07
	Fr	6,26E-09	4,47E-09	3,40E-09	4,02E-09	4,65E-09
	Fn [N]	5,00E-08	5,00E-08	5,00E-08	5,00E-08	5,00E-08
	μ	0,13	0,09	0,07	0,08	0,09

Tip LFMR # 23	Scan size [nm]	100 x 100	100 x 100	100 x 100	100 x 100
	V tip [um/s]	0,4	0,4	0,4	0,4
	Δo/2 [V]	0,013	0,015	0,013	0,016
	Alpha [N/V]	1,79E-07	1,79E-07	1,79E-07	1,79E-07
	Fr	2,39E-09	2,70E-09	2,33E-09	2,78E-09
	Fn [N]	5,00E-08	5,00E-08	5,00E-08	5,00E-08
	μ	0,05	0,05	0,05	0,06

Tip LFMR # 23	Scan size [nm]	100 x 100	100 x 100	100 x 100
	V tip [um/s]	0,4	0,4	0,4
	Δo/2 [V]	0,014	0,014	0,014
	Alpha [N/V]	1,79E-07	1,79E-07	1,79E-07
	Fr	2,55E-09	2,49E-09	2,55E-09
	Fn [N]	5,00E-08	5,00E-08	5,00E-08
	μ	0,05	0,05	0,05

7.1.4 *Quantitative FFM results of V_2O_5 produced by dc reactive magnetron sputtering*

Tip LFMR # 22	Scan size [nm]	1000 x 1000	1000 x 1000	100 x 100	100 x 100
	V tip [µm/s]	2	2	0,4	0,4
	Δo/2 [V]	0,055	0,064	0,076	0,079
	Alpha [N/V]	9,56E-08	9,56E-08	9,56E-08	9,56E-08
	Fr	5,26E-09	6,07E-09	7,24E-09	7,54E-09
	Fn [N]	5,00E-08	5,00E-08	5,00E-08	5,00E-08
	µ	0,11	0,12	0,14	0,15

Tip LFMR # 23	Scan size [nm]	100 x 100	100 x 100	100 x 100	100 x 100	100 x 100
	V tip [µm/s]	0,4	0,4	0,4	0,4	0,4
	Δo/2 [V]	0,024	0,024	0,025	0,021	0,021
	Alpha [N/V]	1,79E-07	1,79E-07	1,79E-07	1,79E-07	1,79E-07
	Fr	4,25E-09	4,29E-09	4,43E-09	3,67E-09	3,82E-09
	Fn [N]	5,00E-08	5,00E-08	5,00E-08	5,00E-08	5,00E-08
	µ	0,08	0,09	0,09	0,07	0,08

Tip LFMR # 23	Scan size [nm]	1000 x 1000	1000 x 1000	1000 x 1000	1000 x 1000	1000 x 1000	1000 x 1000
	V tip [µm/s]	2	2	2	2	2	2
	Δo/2 [V]	0,037	0,038	0,035	0,037	0,037	0,048
	Alpha [N/V]	1,79E-07	1,79E-07	1,79E-07	1,79E-07	1,79E-07	1,79E-07
	Fr	6,64E-09	6,71E-09	6,26E-09	6,53E-09	6,53E-09	8,50E-09
	Fn [N]	5,50E-08	5,00E-08	5,50E-08	6,00E-08	6,00E-08	8,00E-08
	µ	0,12	0,13	0,11	0,11	0,11	0,11

Tip LFMR # 23	Scan size [nm]	500 x 500	500 x 500	500 x 500	500 x 500	1000 x 1000
	V tip [µm/s]	2	2	2	2	2
	Δo/2 [V]	0,042	0,053	0,055	0,043	0,067
	Alpha [N/V]	1,79E-07	1,79E-07	1,79E-07	1,79E-07	1,79E-07
	Fr	7,56E-09	9,39E-09	9,84E-09	7,69E-09	1,19E-08
	Fn [N]	5,00E-08	5,00E-08	5,00E-08	5,00E-08	1,25E-07
	µ	0,15	0,19	0,20	0,15	0,10

Tip LFMR # 24	Scan size [nm]	100 x 100	100 x 100	100 x 100	100 x 100	100 x 100	100 x 100
	V tip [µm/s]	0,4	0,4	0,4	0,4	0,4	0,4
	Δo/2 [V]	0,030	0,027	0,032	0,026	0,029	0,032
	Alpha [N/V]	1,48E-07	1,48E-07	1,48E-07	1,48E-07	1,48E-07	1,48E-07
	Fr	4,43E-09	3,92E-09	4,73E-09	3,80E-09	4,26E-09	4,77E-09
	Fn [N]	5,00E-08	5,00E-08	5,00E-08	5,00E-08	5,00E-08	5,00E-08
	µ	0,09	0,08	0,09	0,08	0,09	0,10

Tip LFMR # 24	Scan size [nm]	1000 x 1000	1000 x 1000	1000 x 1000	1000 x 1000	1000 x 1000
	V tip [µm/s]	2	2	2	2	2
	Δo/2 [V]	0,033	0,038	0,043	0,058	0,027
	Alpha [N/V]	1,48E-07	1,48E-07	1,48E-07	1,48E-07	1,48E-07
	Fr	4,88E-09	5,55E-09	6,35E-09	8,57E-09	3,92E-09
	Fn [N]	5,00E-08	8,00E-08	1,00E-07	1,20E-07	4,00E-08
	µ	0,10	0,07	0,06	0,07	0,10

Tip LFMR # 26	Scan size [nm]	1000 x 1000	1000 x 1000	1000 x 1000	1000 x 1000	1000 x 1000
	V tip [µm/s]	2	2	2	2	2
	Δo/2 [V]	0,058	0,060	0,063	0,066	0,051
	Alpha [N/V]	1,67E-07	1,67E-07	1,67E-07	1,67E-07	1,67E-07
	Fr	9,70E-09	1,00E-08	1,05E-08	1,10E-08	8,44E-09
	Fn [N]	7,20E-08	6,00E-08	8,00E-08	8,00E-08	6,00E-08
	µ	0,13	0,17	0,13	0,14	0,14

Tip LFMR # 26	Scan size [nm]	1000 x 1000	1000 x 1000	1000 x 1000	1000 x 1000	100 x 100	100 x 100
	V tip [µm/s]	2	2	2	2	0,4	0,4
	Δo/2 [V]	0,031	0,043	0,042	0,053	0,046	0,043
	Alpha [N/V]	1,67E-07	1,67E-07	1,67E-07	1,67E-07	1,67E-07	1,67E-07
	Fr	5,18E-09	7,19E-09	6,94E-09	8,86E-09	7,69E-09	7,16E-09
	Fn [N]	6,00E-08	6,00E-08	6,00E-08	6,00E-08	6,00E-08	6,00E-08
	µ	0,09	0,12	0,12	0,15	0,13	0,12

7.1.5 *Quantitative FFM results of V_2O_5 produced by pulsed dc reactive magnetron sputtering*

Tip LFMR # 26	Scan size [nm]	1000 x 1000	1000 x 1000	1000 x 1000	1000 x 1000	1000 x 1000	1000 x 1000
	V tip [um/s]	2	2	2	2	2	2
	Δo/2 [V]	0,045	0,0205	0,0215	0,022	0,024	0,024
	Alpha [N/V]	1,672E-07	1,672E-07	1,672E-07	1,672E-07	1,672E-07	1,672E-07
	Fr	7,52E-009	3,43E-009	3,59E-009	3,68E-009	4,01E-009	4,01E-009
	Fn [N]	8,00E-008	3,50E-08	3,50E-08	3,50E-08	3,50E-08	3,50E-08
	μ	0,09	0,10	0,10	0,11	0,11	0,11

Tip LFMR # 26	Scan size [nm]	1000 x 1000	1000 x 1000	500 x 500	500 x 500	500 x 500	500 x 500
	V tip [um/s]	2	2	1	1	1	1
	Δo/2 [V]	0,0255	0,026	0,040	0,041	0,026	0,023
	Alpha [N/V]	1,672E-07	1,672E-07	1,672E-07	1,672E-07	1,672E-07	1,672E-07
	Fr	4,26E-009	4,35E-009	6,69E-009	6,77E-009	4,26E-009	3,76E-009
	Fn [N]	3,50E-08	3,50E-08	8,00E-008	8,00E-008	4,00E-008	4,00E-008
	μ	0,12	0,12	0,08	0,08	0,11	0,09

Tip LFMR # 26	Scan size [nm]	100 x 100	100 x 100	100 x 100	100 x 100	100 x 100	100 x 100
	V tip [um/s]	0,4	0,4	0,4	0,4	0,4	0,4
	Δo/2 [V]	0,020	0,020	0,020	0,018	0,016	0,013
	Alpha [N/V]	1,672E-07	1,672E-07	1,672E-07	1,672E-07	1,672E-07	1,672E-07
	Fr	3,34E-009	3,34E-009	3,26E-009	2,93E-009	2,59E-009	2,09E-009
	Fn [N]	6,00E-008	6,00E-008	6,00E-008	6,00E-008	6,00E-008	4,00E-008
	μ	0,06	0,06	0,05	0,05	0,04	0,05

7.1.6 Quantitative FFM results of TiN with 7% Ag

Tip LFMR # 22	Scan size [nm]	1000 x 1000	1000 x 1000	1000 x 1000	1000 x 1000
	V tip [um/s]	2	2	2	2
	Δo/2 [V]	0,032	0,040	0,047	0,039
	Alpha [N/V]	9,56E-08	9,56E-08	9,56E-08	9,56E-08
	Fr	3,06E-09	3,77E-09	4,49E-09	3,68E-09
	Fn [N]	5,50E-08	5,50E-08	6,00E-08	5,00E-08
	μ	0,06	0,07	0,07	0,07

Tip LFMR # 23	Scan size [nm]	100 x 100	100 x 100	100 x 100
	V tip [um/s]	0,4	0,4	0,4
	Δo/2 [V]	1,98E-02	2,82E-02	2,87E-02
	Alpha [N/V]	1,788E-007	1,788E-007	1,788E-007
	Fr	3,53E-09	5,03E-09	5,12E-09
	Fn [N]	5,00E-08	7,50E-08	7,50E-08
	μ	0,07	0,07	0,07

Tip LFMR # 24	Scan size [nm]	1000 x 1000	1000 x 1000	1000 x 1000	100 x 100	100 x 100	100 x 100
	V tip [um/s]	2	2	2	0,4	0,4	0,4
	Δo/2 [V]	0,045	0,037	0,043	0,031	0,030	0,026
	Alpha [N/V]	1,478E-007	1,478E-007	1,478E-007	1,478E-007	1,478E-007	1,478E-007
	Fr	6,65E-009	5,39E-009	6,28E-009	4,51E-009	4,36E-009	3,89E-009
	Fn [N]	1,10E-007	1,00E-007	8,00E-008	6,00E-008	6,00E-008	6,00E-008
	μ	0,06	0,05	0,08	0,08	0,07	0,06

Tip LFMR # 26	Scan size [nm]	100 x 100	100 x 100	100 x 100	1000 x 1000
	V tip [um/s]	0,4	0,4	0,4	2
	Δo/2 [V]	0,028	0,026	0,023	0,036
	Alpha [N/V]	1,672E-007	1,672E-007	1,672E-007	1,672E-007
	Fr	4,69E-009	4,32E-009	3,82E-009	6,02E-009
	Fn [N]	8,00E-008	7,60E-008	7,00E-008	8,00E-008
	μ	0,06	0,06	0,05	0,08

7.1.7 *Quantitative FFM results of pure TiN*

Tip LFMR # 23	Scan size [nm]	1000 x 1000	1000 x 1000	1000 x 1000	1000 x 1000	500 x 500	500 x 500
	V tip [µm/s]	2	2	2	2	1	1
	Δo/2 [V]	0,020	0,028	0,038	0,022	0,017	0,017
	Alpha [N/V]	1,79E-07	1,79E-07	1,79E-07	1,79E-07	1,79E-07	1,79E-07
	Fr	3,57E-09	5,01E-09	6,71E-09	3,87E-09	3,09E-09	3,06E-09
	Fn [N]	6,00E-08	8,00E-08	8,00E-08	6,00E-08	6,00E-08	6,00E-08
	µ	0,06	0,06	0,08	0,06	0,05	0,05

Tip LFMR # 23	Scan size [nm]	100 x 100	100 x 100	100 x 100	100 x 100	100 x 100
	V tip [µm/s]	0,4	0,4	0,4	0,4	0,4
	Δo/2 [V]	0,031	0,030	0,027	0,021	0,028
	Alpha [N/V]	1,79E-07	1,79E-07	1,79E-07	1,79E-07	1,79E-07
	Fr	5,54E-09	5,28E-09	4,81E-09	3,83E-09	5,04E-09
	Fn [N]	8,00E-08	8,00E-08	8,00E-08	7,00E-08	6,00E-08
	µ	0,07	0,07	0,06	0,05	0,08

Tip LFMR # 23	Scan size [nm]	100 x 100	100 x 100	100 x 100	100 x 100
	V tip [µm/s]	0,4	0,4	0,4	0,4
	Δo/2 [V]	0,028	0,028	0,023	0,021
	Alpha [N/V]	1,79E-07	1,79E-07	1,79E-07	1,79E-07
	Fr	4,99E-09	4,98E-09	4,18E-09	3,76E-09
	Fn [N]	6,00E-08	6,00E-08	7,00E-08	7,00E-08
	µ	0,08	0,08	0,06	0,05

Tip LFMR # 22	Scan size [nm]	1000 x 1000	1000 x 1000	500 x 500	500 x 500	500 x 500	500 x 500
	V tip [µm/s]	2	2	1	1	1	1
	Δo/2 [V]	0,020	0,019	0,019	0,018	0,017	0,016
	Alpha [N/V]	9,56E-08	9,56E-08	9,56E-08	9,56E-08	9,56E-08	9,56E-08
	Fr	1,93E-09	1,78E-09	1,83E-09	1,72E-09	1,61E-09	1,57E-09
	Fn [N]	5,00E-08	5,00E-08	5,00E-08	5,00E-08	5,00E-08	5,00E-08
	µ	0,04	0,04	0,04	0,03	0,03	0,03

Tip LFMR # 22	Scan size [nm]	100 x 100	100 x 100	100 x 100	100 x 100
	V tip [µm/s]	0,4	0,4	0,4	0,4
	Δo/2 [V]	0,029	0,028	0,027	0,026
	Alpha [N/V]	9,56E-08	9,56E-08	9,56E-08	9,56E-08
	Fr	2,74E-09	2,64E-09	2,61E-09	2,44E-09
	Fn [N]	7,50E-08	7,50E-08	7,50E-08	7,50E-08
	µ	0,04	0,04	0,03	0,03